



Characterizing turbulent boundary layer response and recovery to buffer region spanwise blowing

Andrew Meyers¹, Alan Duong¹, Thomas C. Corke¹  and Flint O. Thomas¹ 

¹Institute for Flow Physics and Control, Aerospace and Mechanical Engineering Department, University of Notre Dame, Notre Dame, IN 46556, USA

Corresponding author: Thomas C. Corke, tcorke@nd.edu

(Received 20 June 2024; revised 14 May 2025; accepted 15 May 2025)

Experiments were performed that (i) document the effect of the steady spanwise buffer layer blowing on the mean characteristics of the turbulent boundary layer for a range of momentum thickness Reynolds numbers from 4760 to 10 386, and (ii) document the effect of the buffer layer blowing on the unsteady characteristics and coherent vorticity in a boundary layer designed to provide sufficiently high spatial resolution. The spanwise buffer layer blowing of the order of u_τ is produced by a surface array of pulsating direct current (pulsed-DC) plasma actuators. This was found to substantially reduce the wall shear stress that was directly measured with a floating element coupled with a force sensor. The direct wall shear measurements agreed with values derived using the Clauser method to within $\pm 0.85\%$. The degree to which the buffer layer blowing affected τ_w was found to primarily depend on the inner variable spanwise spacing between the pulsed-DC actuator electrodes, i.e. ‘blowing sites’. Utilizing pairs of $[u, v]$ and $[u, w]$ hot-wire sensors, the latter experiments correlated significant reductions in the ω_y and ω_x vorticity components that resulted from the buffer layer blowing and translated into lower Reynolds stresses and turbulence production. The time scale to which these observed changes in the boundary layer characteristics would return to the baseline condition was subsequently documented. This revealed a recovery length of $x^+ \approx 86\,000$ that translated to a streamwise fetch of $x \approx 66\delta$. Finally, a comparison with the recent work by Cheng *et al.* (2021, *J. Fluid Mech.* vol. 918, A24) and Wei & Zhou (2024 in *TSFP13*, June 25–28, 2024) that followed our experimental approach to achieve comparable wall shear stress (drag) reductions has led to a new scaling based on the baseline boundary layer Re_τ and buffer layer blowing velocity.

Key words: boundary layer control, boundary layer structure

1. Introduction

The early observations by Kline *et al.* (1967) of near-wall low speed streaks in turbulent boundary layers (TBLs) has led to a consensus that a cycle of ‘liftup and breakup’ of fluid within the buffer layer plays a key role in turbulence production (Corino & Brodkey 1969), and is correlated with high levels of viscous drag (Kline *et al.* 1967; Kim 2011). Jimenez & Moin (1991), Hamilton, Kim & Waleffe (1995), Jimenez & Pinelli (1999) and Schoppa & Hussain (2002), among others, suggest that there exists a near-wall autonomous cycle that is responsible for the generation and growth of streamwise near-wall vorticity.

Early theoretical models for a regenerative bursting process based on the instability of the sublayer were proposed by Hanratty (1956), Einstein & Li (1956) and Black (1966). According to their analysis the bursting frequency should scale with inner wall variables, u_τ^2/ν . This contradicted Rao, Narashima & Narayanan (1971), who suggested that the burst frequency scaled with outer variables, thereby suggesting an influence of the outer large-scale motions in the boundary layer. Doligalski, Smith & Walker (1980) proposed a model for the liftup of low-speed fluid from the wall that was based on the interaction with an eddy structure that originated in the outer part of the boundary layer.

The interaction between outer large-scale coherent motions and near-wall fine scale turbulence is also widely recognized. Hutchins & Marusic (2007a) and Hutchins & Marusic (2007b) demonstrated that near-wall turbulence is modulated by the outer large-scale motions. This amplitude modulation of near-wall turbulence was further characterized by Mathis, Hutchins & Marusic (2009) and Mathis, Hutchins & Marusic (2011). The influence of the modulation of near-wall turbulence by outer region coherent motions has been shown to increase with Reynolds number as these outer layer structures become progressively more energetic. Thus, the influence of the outer structures on near-wall turbulence is expected to grow with Reynolds number. Investigations on the role of large-scale motions away from the wall in TBLs (Robinson 1991) have motivated investigations by Corke, Nagib & Guezennec (1981) and Savill & Mumford (1988) to document the impact that suppression of the outer large-scale dynamics would have on the near-wall dynamics.

The significant role played by coherent streamwise buffer layer vorticity in TBLs is also widely acknowledged (Kline *et al.* 1967; Blackwelder & Eckelman 1979; Robinson 1991). These play a key role in turbulent skin-friction drag as noted by Kim (2011), among others. These near-wall vortices serve to transfer high momentum fluid to the wall on one flank which serves to steepen the wall-normal gradient of streamwise velocity and thereby enhance friction drag and heat transfer. Low speed fluid is transferred away from the wall on the other flank and gives rise to a gradient reduction effect above the wall (Schoppa & Hussain 2002).

Blackwelder & Woo (1974) investigated the burst process by applying a pressure perturbation that was designed to simulate a passing large eddy. This yielded no change in the burst frequency. Numerical experiments on turbulent channel flow by Jimenez & Pinelli (1999) showed quite convincingly that a near-wall turbulence production cycle exists, which is essentially independent of the outer flow. This was demonstrated by artificially manipulating the outer flow in numerical simulations and observing the resulting effect on near-wall turbulence production. The manipulation of the outer flow was found to have little effect on the near-wall turbulence generation process, thereby suggesting its autonomous character. Similarly, it was shown that the turbulence generation mechanism was not directly linked to the presence of the wall; the wall served only to provide the necessary mean shear.

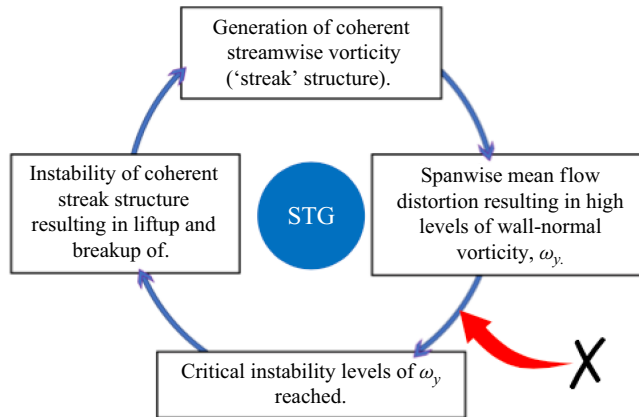


Figure 1. Autonomous near-wall cycle involving liftup and breakup of coherent streamwise vorticity associated with the low-speed wall streak structure and near-wall turbulence production of which spanwise sublayer blowing is intended to intervene.

Schoppa & Hussain (1998) proposed a large-scale strategy for skin friction drag reduction that was demonstrated in a direct numerical simulation (DNS) of a turbulent channel flow. In that, they imposed a streamwise-independent, near-wall spanwise velocity component along the channel wall by means of either a pair of counter-rotating streamwise vortices, or opposed wall jets. In these simulations, a spanwise velocity component of 6 % of the channel centreline velocity produced respective reductions in the skin friction of 20 % and 50 % for the counter-rotating vortices and opposed wall jets.

Canton, Orlu & Schlatter (2016) repeated the channel DNS simulations performed by Schoppa & Hussain (1998) in which they aimed to further characterize the physics governing the drag reduction control, as well as well as investigating optimum parameters. Their simulations were performed at the same and higher friction Reynolds numbers $Re_\tau = u_\tau h / \nu$ as Schoppa & Hussain (1998), where u_τ is the friction velocity, h is the channel half-height and ν is the kinematic viscosity. They achieved drag reduction for the $Re_\tau = 104$ and 180 cases that were formerly investigated by Schoppa & Hussain (1998). However, they did not observe drag reduction in their simulations at $Re_\tau = 550$. From that, they concluded that the original implementation of Schoppa & Hussain (1998) does not lead to sustained drag reduction but is rather a ‘transient feature’ that is limited to low Re_τ conditions.

In response, Yao *et al.* (2017) concluded that because the controlling swirl flow in the Canton *et al.* (2016) simulations was fixed at the centre of the channel, their observed disappearance of the drag reduction at $Re_\tau = 550$ was due to the inability of the control flow to sufficiently influence the viscous sublayer and thereby intervene in the streak transient growth mechanism. With the caveat that the flow control needed to be confined to the buffer layer, the Yao *et al.* (2017) results showed effective drag reductions of 19 %, 14 % and 12 % at $Re_\tau = 180$, 395 and 550, respectively. This subsequently opposed the suggested lack of effectiveness with increasing Reynolds number postulated by Canton *et al.* (2016). These results suggested that significant drag reduction can be achieved if the control flow is specifically targeted to the buffer layer, and properly accounts for its thinning with increasing Reynolds number. This result was a key takeaway employed in our experiments.

The flow control strategy we employ in this study is motivated by the autonomous near-wall cycle schematically illustrated in figure 1. In this, the pumping action of quasisteady streamwise vortices associated with the near-wall streak structures (Kline *et al.* 1967) gives

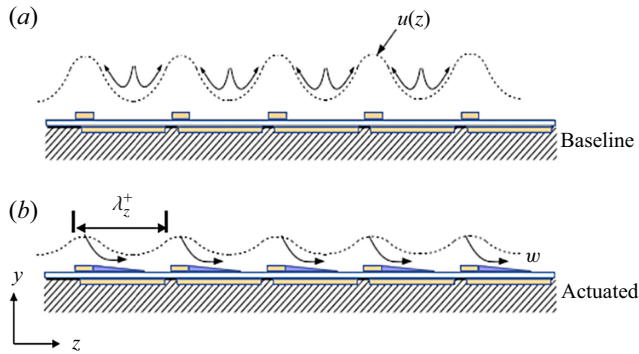


Figure 2. Schematic representation of spanwise mean-flow distortion, $u(z)$ in baseline boundary layer (a) and surface mounted plasma actuator array (b) to produce steady uniform sublayer blowing designed to reduce the mean flow distortion. Electrode thickness is exaggerated for clarity.

rise to near-wall spanwise mean flow distortion that is unstable to disturbances and results in a cycle of liftup and breakup of low-speed fluid from the wall. Following Schoppa & Hussain (2002), the magnitude of the wall-normal vorticity, ω_y , is a critical parameter that controls this cycle of events.

Our flow control approach seeks to interrupt this cycle by reducing the spanwise mean flow distortion below a critical level. As illustrated in figure 2, it involves generating a steady predominantly spanwise velocity component of the order of u_τ , that is confined within the buffer layer using an array of wall-mounted pulsating direct current (pulsed-DC) plasma actuators. A similar approach using alternating current (AC) plasma actuators was recently performed by Cheng *et al.* (2021) and Wei & Zhou (2024).

The spanwise buffer layer blowing is not significantly different from the effect of an oscillating wall or body force. Experiments and numerical simulations with oscillating walls (Baron & Quadrio 1996; Trujillo, Bogard & Ball 1997; Dhanak & Si 1999; Choi & Clayton 2001; Choi, Chun-Xiao & Sung 2002) had observed as much as a 40 % drag reduction, with a corresponding 70 % reduction in u'/U_∞ . Quadrio & Sibilla (2011) showed that the space-averaged spanwise oscillating flow is consistent with the laminar Stokes layer solution, which in the mean is equivalent to spanwise blowing. In cases showing drag reduction, the thickness of the Stokes layer was only a few wall units, which points to an interaction between the Stokes layer and the near-wall low-speed streaks as the basis for the reduced drag. A detailed review of the effects of an oscillating wall on TBLs is provided by Ricco, Skote & Leschziner (2021).

This background had motivated a number of objectives for the work presented in this manuscript. Given the apparent controversy between Schoppa & Hussain (1998) and Canton *et al.* (2016) that was addressed by Yao *et al.* (2017), one important objective was to document the effect of the spanwise buffer layer blowing on the mean boundary layer characteristics, including the viscous shear stress, for an extensive range of higher Re_τ values.

With the recent results of Cheng *et al.* (2021) and more importantly Wei & Zhou (2024) who employed a similar experimental approach at lower Re_τ values comparable to those in the Yao *et al.* (2017) simulations, we intended to further examine the scaling of the spanwise blowing effect on Re_τ .

Although the reduction in viscous shear stress has obvious practical implications (e.g. Thomas, Corke & Duong 2023), the focus of this work was on further documenting the effect of the spanwise buffer layer blowing on the turbulence characteristics and production. Of particular interest was measuring the change in the magnitude of the

wall-normal vorticity component, ω_y , that occurred with the spanwise blowing and was considered a critical control parameter (Schoppa & Hussain 2002). This would be accomplished in a boundary layer designed to produce good spatial resolution for dual-sensor, $[u, v]$ and $[u, w]$ hot-wire measurements. These data would be used to measure wall-normal Reynold stress distributions and turbulence production. In addition it would measure the effect of the buffer layer blowing on the frequency and strength of turbulence producing low-speed fluid liftup and breakup events.

The detection of the turbulence producing events would be used as a condition to perform three-dimensional (3-D) spatial ensembles of coherent motions from which ω_x and ω_y distributions could be constructed. Based on Schoppa & Hussain (2002), the latter is important in quantifying the impact of our spanwise blowing approach. The buffer layer streamwise vorticity component, ω_x , is emblematic of the near-wall longitudinal vortical structures that are the presumed source of the spanwise mean flow distortion that we wish to reduce.

Another point of interest was the convective distance or time scale over which the boundary layer characteristics recovered from the termination of the buffer layer blowing. The resulting time scale was intended to shed light on the mechanism(s) for turbulence production in the boundary layer such as being based on inner variables that might support a so-called ‘bottom up’ process, or being based on the boundary layer outer variables that might support a so-called ‘top down’ process, or possibly a mix of both processes.

With this in mind, transient experiments would be performed in which a steady-state condition with spanwise buffer layer blowing would be terminated to allow the boundary layer to return to its nominal baseline state. The time scale for this to occur will be based on the recovery of measured boundary layer characteristics that were found to be correlated with the buffer layer blowing, including turbulence velocity fluctuation and turbulence production levels, frequency of low-speed fluid liftup and breakup events, viscous shear stress, etc. For reference, Schoppa & Hussain (1998) had indicated that the region of sustained drag reduction would extend to $x^+ \simeq 16\,000$. In direct drag measurements using oil film interferometry, Thomas *et al.* (2019) found good agreement with that prediction. However, this was for an earlier case where the actuator was less optimized, producing only a 6 % reduction in u_τ . The recovery time scale starting from a significantly larger initial u_τ reduction will provide further insight on the effect of the starting condition.

Throughout these experiments, the buffer layer blowing is regarded as a ‘tool’ with which potential mechanisms for the observed drag reduction can be evaluated.

2. Experimental set-up

The experiments were performed in two different wind tunnel facilities in the Notre Dame Hessert Laboratory for Aerospace Research. Both wind tunnels are closed-return designs with turbulence management that results in free stream turbulence levels (u'_{rms}/U_∞) of 0.05 %. The test sections in both wind tunnels have the same dimensions with a 0.91 m square cross-section and a length of 2.73 m. Both test sections have three square 0.61 m windows on all four sides. Besides offering excellent optical access for laser-based measurements, they are also removable to provide hard-points for mounting probes and in the case of these experiments, a floating element drag measurement surface.

The free stream velocity in both facilities is adjustable. One of the wind tunnels has a maximum free stream Mach number of 0.6 (204 m s^{-1}). In this tunnel, the free stream temperature is controllable and can be held constant to within 1°C . The other wind tunnel has a maximum free stream Mach number of 0.15 (51 m s^{-1}). The free stream temperature in this tunnel is allowed to stabilize before taking measurements.

Mach 0.6 tunnel boundary layers	
U_∞ (m s ⁻¹)	17–51
u_τ (m s ⁻¹)	0.67–1.78
δ (mm)	55–40
Re_x	2.8×10^6 – 8.1×10^6
Re_θ	4760–10 386
Mach 0.15 tunnel boundary layer	
U_∞ (m s ⁻¹)	4.6
u_τ (m s ⁻¹)	0.17
δ (mm)	140
Re_x	7.25×10^5 – 8.1×10^6
Re_θ	2500

Table 1. Experimental conditions.

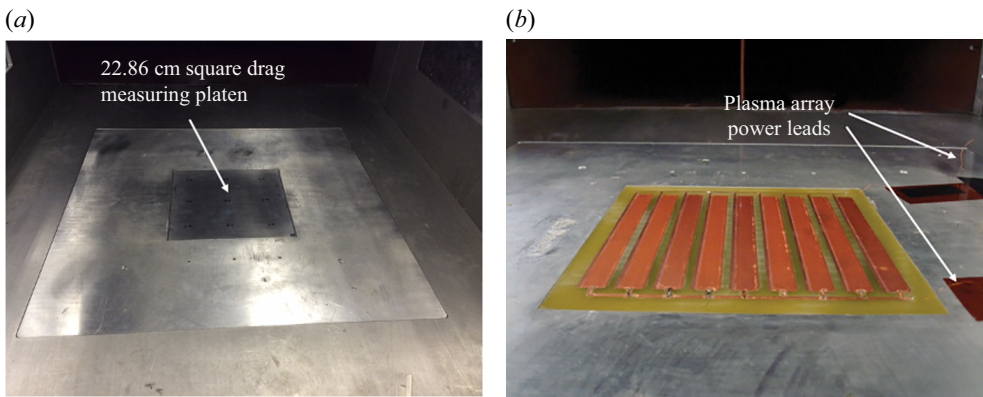


Figure 3. Photographs of drag measuring platen with smooth surface used in baseline boundary layer measurement (a) and with plasma actuator array installed on the platen surface (b).

In each wind tunnel, the TBL is developed on the test-section floor. In the Mach 0.6 tunnel, the turbulence transition location was established by a two-dimensional (2-D) sandpaper strip that was located at the entrance of the test section. In that case, the boundary layer thickness, δ , at the downstream end of the test section, based on the free stream velocity, ranged from 40 to 55 mm. In the lower-speed tunnel, the boundary layer was thickened by the addition of uniformly spaced 2-D roughness elements that covered the first 0.3 m (11 %) of the test section floor. This is a common approach used in atmospheric boundary layer simulations (Tan-atichat & Nagib 1976). The ‘2-D’ roughness consisted of eight 19 mm square cross-section aluminium bars placed in a spanwise orientation across the full width of the test section with 3.8 cm spacing, and 18 6.4 mm square cross-section aluminium bars that rested on top of the other bars, aligned in the streamwise direction and spaced 3.8 cm apart. The boundary layer thickness at the downstream location was 140 mm. The boundary layer baseline characteristics for both sets of experiments are given in table 1.

In both wind tunnels, the velocity and air temperature were, respectively, monitored by a Pitotstatic probe and temperature sensor at the downstream location where the boundary layer measurements were performed. The same floating element drag measuring platen replaced the most downstream window location in the floor of the wind tunnel test sections.

Photographs of the drag measuring platen in the wind tunnel floor are shown in [figure 3](#). [Figure 3\(a\)](#) shows the platen without the pulsed-DC actuator array. [Figure 3\(b\)](#) shows the plasma actuator array covering the platen surface. The platen is a 22.86 cm square that is located in the centre span of the wind tunnel test section. The platen is mounted on linear air bearings that only allow motion in the streamwise direction and therefore is only capable of measuring the streamwise component of the wall shear stress.

Interchangeable cantilever-style load cells were used to measure the total wall shear stress that acted over the platen surface area, both as a smooth surface or when covered by the plasma actuator array. The load cell used for the velocity range $17\text{--}51\text{ m s}^{-1}$ was chosen to have a high resolution across that range, with a maximum rated output of 2 N (204 g). The load cell had a hysteresis of 0.03 % of the rated output (204 g) and a non-repeatability of 0.05 % of the rated output. Propagating these uncertainties, the total uncertainty was 0.06 % of the rated output or approximately 0.12 g. The drag force for these baseline boundary layer measurements was expected to vary from 3 to 22 g, and therefore the maximum uncertainty in the drag measurements was approximately 4 % at the lowest speed and 0.06 % at the highest speed.

In the low-speed experiment ($U_\infty = 4.6\text{ m s}^{-1}$) used to document the changes in the TBL coherent structures under the influence of the spanwise buffer layer blowing, the selected load cell had a maximum rated load of 0.5 N (51 g). This had an accuracy of 0.05 % of the maximum rated load which translated to a measurement uncertainty of 0.025 g.

The drag measurement system was calibrated by hanging known weights in a pulley arrangement that would produce a translational force on the platen. The calibration was performed before and after each day of wind tunnel runs. In an early validation of the direct drag measurement approach, Jasinski & Corke (2020) using the same force balance with a smooth platen surface matched the Coles–Fernholz relation (Baars *et al.* 2016) to within 1 % over a wide range of Re_θ .

The height of the actuator array surface relative to the tunnel floor is adjustable at four points. This was maintained to be flush with the tunnel floor to within $\pm 0.2\text{ mm}$. A 0.508 mm gap surrounds the platen. By design, pressure in the wind tunnel test section is slightly above the outside atmospheric pressure. To prevent air from leaking around the gap that could affect the shear stress measurement, the area under the drag platen assembly including the air bearings and load cells is fully enclosed and sealed to prevent any air leaks through the gap and into the laboratory space.

As shown in [figure 3\(b\)](#), the plasma actuator array covered the surface of the drag force measurement platen. For the higher velocity experiments, it consisted of nine plasma actuators spaced 22 mm apart and connected in parallel to the pulsed-DC power source. The electrodes consisted of 0.106 mm thick dead-soft copper foil tape. The foil tape of the exposed electrodes was lapped to approximately half its original thickness, where depending on the free stream speed, the thickness corresponded to a $2.5 \leq y^+ \leq 7.5$.

In the [figure 3\(b\)](#) photograph, the exposed electrodes are the narrow strips aligned in the flow direction. These are on the top surface of the dielectric material. The covered electrodes are the wider copper strips with one each per exposed electrode. These appear as a dull copper colour because they are being viewed through the translucent dielectric material layer. As shown in the schematic in [figure 2\(a\)](#), one side edge of the exposed and covered electrodes overlap slightly. The dielectric layer was a 22.86 cm square by 0.1016 mm-thick sheet of V2-quality muscovite mica. The underside of the mica was backed by a 0.0254 mm thick sheet of Kapton film. The mica sheet was used because it has excellent dielectric properties that do not degrade over time when subjected to the ionized air. The complete plasma actuator array was bonded to a 25.4 mm-thick Garolite sheet. The Garolite sheet was subsequently mounted to the surface of the platen.

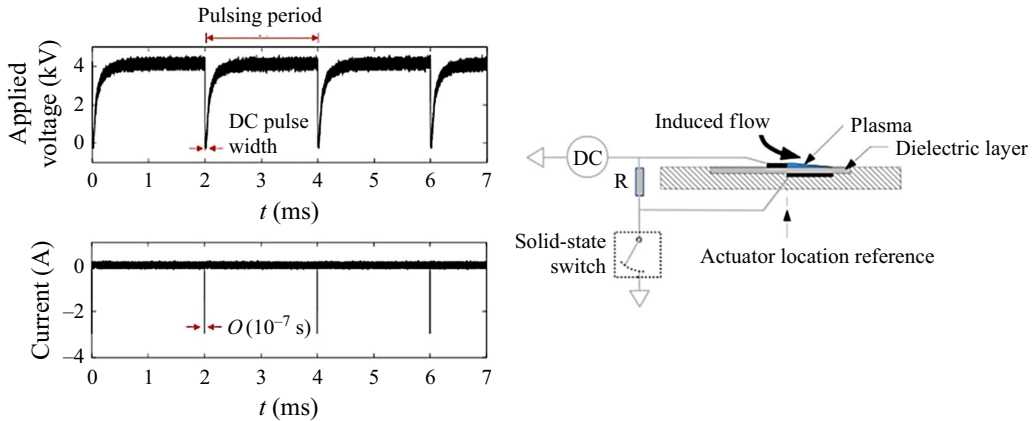


Figure 4. Pulsed-DC circuit schematic and sample voltage and current waveforms.

The plasma actuator array was powered by a pulsed-DC circuit. A circuit schematic and sample voltage and current waveforms are shown in figure 4. In this approach, a direct current (DC) voltage is supplied to both the exposed and covered electrodes. With the dielectric layer separating the two electrodes, the actuator is electrically equivalent to a capacitor. As such, it will only pass a time-varying current. This was produced by periodically shorting to ground the connection to the covered electrode using a solid-state switch. It is only during this instant, which is designed to be extremely short, $O(10^{-7})$ s, that the actuator draws power. The extremely low current supplied to the plasma actuator is evident by the small gauge and barely visible power leads that are pointed out in figure 3(b). In the results to follow, the maximum power supplied to the actuator array was 7.47 W which when distributed over the 0.524 m^2 array corresponded to 0.014 W m^{-2} . To allay any concern about heating effects of the plasma array on wall shear stress measurements, in the worst case of the lowest 4.6 m s^{-1} free stream velocity and an air temperature of 26° C , and assuming 100 % of the power is converted to heat, it would only account for 0.7 % of the heat content in the air stream. The effect is even less at the higher free stream speeds of the experiment, and would produce a negligible effect on the boundary layer.

In the results that follow, the pulsing frequency was 500 Hz. Preliminary experiments performed in ambient air (Duong 2019) indicated that this induced a steady velocity distribution similar to a tangential wall jet. Importantly, the 500 Hz was not related to any outer or inner characteristic time scales of the baseline TBL.

In the early stages of our research campaign, we were also concerned with any effect of electronic noise or even electrostatic forces that would affect the drag measurements. To allay these concerns, measurements were taken with the plasma actuator operating without wind tunnel flow. The force balance is not sensitive to any lateral thrust (although imperceptible) produced by the actuator so that any effect of electronic noise or electrostatic force could be determined. Through this process, procedures were developed for wire shielding and shielding around the load cell. In addition, it was noticed that an electrostatic force was evident. This resulted from the voltage potential between a bus line powering the exposed electrodes, and the earth-grounded metal tunnel floor. This was eliminated by increasing the distance between the bus line and the edge of the platen. With these procedures, no measurable effects of electronic noise or electrostatic forces remained. All subsequent experiments followed these procedures.

The single and dual hot-wire sensors used in the experiment were all operated in a constant temperature anemometer mode using a specially designed circuit that allowed the reference ground to float. Details of the constant temperature anemometer circuit are given by Duong (2019). The floating ground design is essential for operating hot-wires in the weakly ionized (typically less than 1 p.p.m. weakly ionized gas (Corke, Enloe & Wilkinson 2010)) air stream directly downstream of the plasma actuator array. Otherwise a charge build-up on the hot-wire sensors will generate a current through the sensor that will cause it to immediately fail. Early applications of a floating constant-current anemometer design were in boundary layer measurements at Mach 3.5 by Matlis (2003) and low-pressure turbine cascade experiments by Huang, Corke & Thomas (2006a) and Huang, Corke & Thomas (2006b).

In the floating ground constant temperature anemometer design used in these experiments, the entire anemometer circuit was isolated by utilizing two 12 VDC car batteries as voltage sources. A fibre-optic coupling was also included to further provide isolation between the anemometer floating ground and the instrument ground of the digital data acquisition system and monitoring instrumentation.

Hot-wire calibration was performed by placing the sensor probes in the core of a calibration jet with known velocities. For the dual sensor probes, the probes were rotated through multiple angles in the calibration jet. The calibration voltage–angle–velocity data triplets were used in a look-up table to convert the anemometer voltage to velocity in the experiments. Any differences between the calibration temperature and the wind tunnel temperature, which was generally constant to within 1 °C, was corrected prior to hot-wire voltage conversion to velocity. Based on the calibration, the uncertainty in the mean u (based on the lower wire of the $[uw]$ sensor for spatial reasons) was approximately 1 %. The combination of calibration uncertainty and spatial resolution gave an estimated accuracy of the rms levels of the three velocity at approximately 5 %.

In the experiments, the time series sampling rate was 25 kHz. To prevent frequency aliasing, the digitized time series were first passed through analogue fourth-order low pass filters with a cutoff frequency of 10 kHz.

3. Results

The results to be presented are divided into two primary parts. The first part documents the effect of the spanwise buffer layer blowing in the mean (time-averaged) characteristics of the boundary layer. For this, the experiments were conducted in the Mach 0.6 Wind Tunnel. The baseline conditions were given in table 1. The second part documents changes in the coherent structures of the TBL that result from the spanwise blowing as well as the temporal response of the mean and unsteady characteristics when the spanwise buffer layer blowing was terminated. These experiments were performed in the Mach 0.15 Wind Tunnel of which the baseline boundary layer conditions were also given in table 1.

3.1. Time-averaged boundary layer characteristics

This section documents the effect of the spanwise buffer layer blowing on the mean characteristics of the TBLs over a range of momentum thickness Reynolds numbers from $4760 \leq Re_\theta \leq 10\,386$. The measurements were taken with a hot wire that was located on the test section spanwise centreline, 1 cm downstream of the drag measuring platen. The actuator array was located on the platen but not operated for the baseline boundary layer measurements.

The conditions in the wind tunnel test section were monitored with a Pitotstatic probe and a temperature sensor located in the free stream. Their voltage outputs were

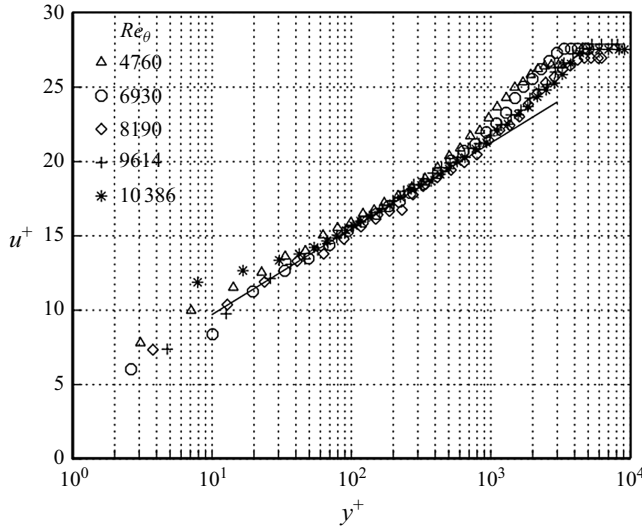


Figure 5. Mean velocity profiles of baseline TBLs at different momentum thickness Reynolds numbers with velocity and wall-normal values scaled by inner variables. Solid curve denotes the log-law of the wall.

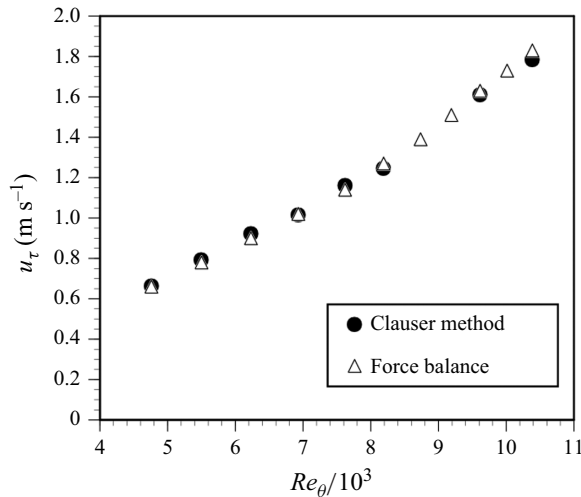


Figure 6. Comparison between shear velocity of the baseline TBLs determined from the drag measuring platen and with the Clauser method for different momentum thickness Reynolds numbers.

simultaneously recorded with the voltage time series from the drag platen load cell, and hot-wire sensors. The hot-wire anemometer voltage time series was sampled at 25 kHz for 30 s. Multiple records were taken to build up converged statistical averages. The measurements were taken with the plasma actuator sequentially off and on without changing the free stream velocity. The actuator off condition represents the baseline condition. This was repeated for each momentum thickness Reynolds number case.

Figure 5 shows mean velocity profiles of the baseline TBLs at different momentum thickness Reynolds numbers with the velocity and wall-normal values scaled by inner variables, v and $u_\tau = (\tau_w/\rho)^{1/2}$. The baseline shear stress, τ_w , used in the scaling in the figure was derived from the drag measuring platen. For this, the total force measured by the load cell was divided by the surface area of the platen to obtain τ_w .

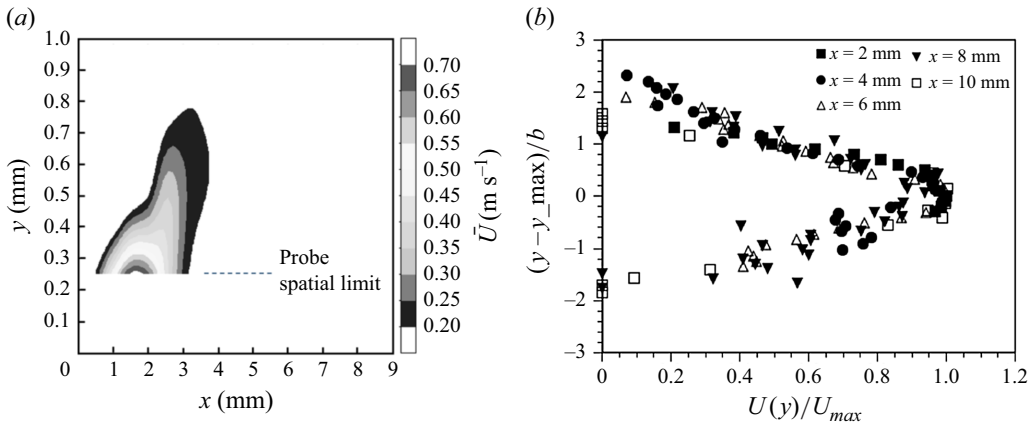


Figure 7. Constant level velocity contours (a) and normalized wall-normal profiles (b) of mean velocity field generated by a pulsed-DC plasma actuator in still air: $V_{DC} = 4$ kV; $f = 500$ Hz.

Alternatively, the Clauser method was applied to the mean profiles to obtain the shear stress used in determining the values of u_τ . A comparison of the shear velocities obtained by the two methods is shown in figure 6. Over the full range of TBL cases, the average difference in the u_τ values obtained by the two measurement approaches was $\pm 0.85\%$. As will be shown, the effect the spanwise blowing has on the mean velocity profile will prevent the use of the Clauser method for determining the wall shear stress. Therefore, in those cases, the wall shear stress is determined with the drag measuring platen.

As previously discussed, Yao *et al.* (2017) had emphasized the importance of having the control flow specifically targeting the buffer layer of the TBL. With that motivation, Duong (2019) had performed experiments with the pulsed-DC plasma actuator over a range of DC voltages to determine the velocity and spatial distribution of the induced mean flow in still air. These velocity measurements were obtained in a quiescent environment with a glass total pressure Pitot probe that was mounted on a two-component (x , y) micrometer traversing mechanism in a separate actuator test facility. The measurement tip of the glass probe was drawn to an inside diameter of approximately 0.15 mm. This could measure to a minimum distance from the surface of $y_{min} = 0.2$ mm. The total pressure was measured using a differential pressure transducer with the reference port open to the room atmosphere. A representative example of the mean velocity spatial distribution from the pulsed-DC actuator is shown in figure 7(a). For this, the DC voltage was 4 kV and the pulsing frequency was 500 Hz. This shows constant level contours of the mean x -component velocity as a function of the 2-D spatial dimensions. The x dimension is the distance from the plasma-forming edge of the actuator exposed electrode. It is aligned parallel to the surface. The y -dimension is aligned perpendicular to the surface. The normalized wall-normal profiles shown in figure 7(b) document that the pulsed-DC actuator serves to produce a compact, self-similar wall jet when operated in a quiescent environment.

It is evident in figure 7 that the majority of the induced velocity field resides close to the surface and quickly decays a short distance from the exposed electrode. The peak velocity, \bar{U}_{max} , is centred at $y \approx 0.25$ mm and $x \approx 1.75$ mm. These dimensions and peak velocity, now indicated as the spanwise velocity \bar{W}_{max} appropriate to our application, are displayed in table 2 when normalized by inner variables for the baseline TBLs at the different free stream velocities and corresponding momentum thickness Reynolds numbers. This indicates that for these cases, the majority of the plasma actuator induced velocity is

U_∞	Re_θ	$y^+ @ \overline{W}_{max}$	$z^+ @ \overline{W}_{max}$	$\overline{W}_{max}/u_\tau$
17.2	4760	11.1	77.9	1.22
20.6	5500	13.1	91.7	1.03
24.0	6230	15.2	106.3	0.89
27.4	6930	17.2	120.4	0.79
30.9	7620	19.2	134.6	0.70
34.3	8190	21.5	150.3	0.63
37.7	8735	23.5	164.5	0.58
41.2	9190	25.5	178.5	0.53
44.6	9614	27.5	192.5	0.49
48.0	10013	29.2	204.1	0.46
51.5	10386	30.9	216.5	0.44

Table 2. Pulsed-DC plasma actuator induced spatial velocity field characteristics normalized by inner variables.

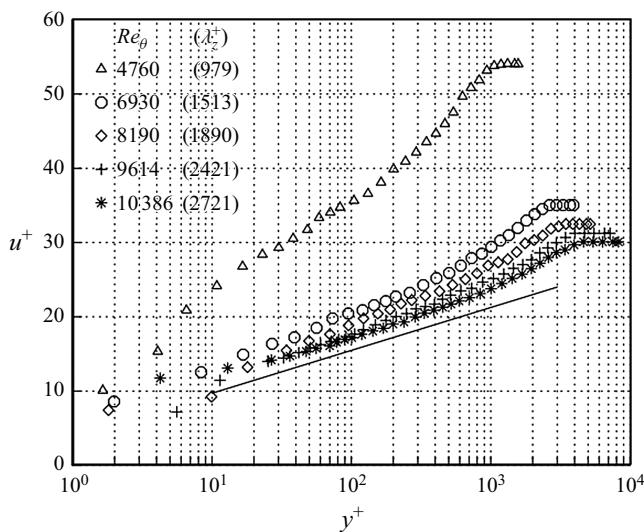


Figure 8. Mean velocity profiles with spanwise buffer layer blowing in the TBLs at different momentum thickness Reynolds numbers with velocity and wall-normal values scaled by inner variables. Actuator voltage was 8 kV. The line is from baseline boundary layers in figure 5.

confined within the buffer layer, and that the peak velocity is of the order of the friction velocity, u_τ .

Having confirmed that the induced mean flow from the pulsed-DC actuator array is confined to the buffer layer of the turbulent boundary, the effect this had on the inner-variable scaled mean velocity profiles is shown in figure 8. The actuator voltage for each of these profiles was fixed at 8 kV. The inset label in the figure lists the corresponding momentum thickness Reynolds number, which can be equated to the respective free stream velocities in table 2. Also listed for each profile are the effective spanwise spacing between electrodes in inner variables, λ_z^+ . We note that these spacings are generally an order of magnitude larger than the z^+ distances (λ_z^+ in the boundary layer) of the peak actuator induced velocities listed in table 2.

As shown in figure 8, the spanwise buffer layer blowing resulted in a reduction of the wall shear stress that is reflected in a lowering of the wall shear velocity, u_τ . This produced

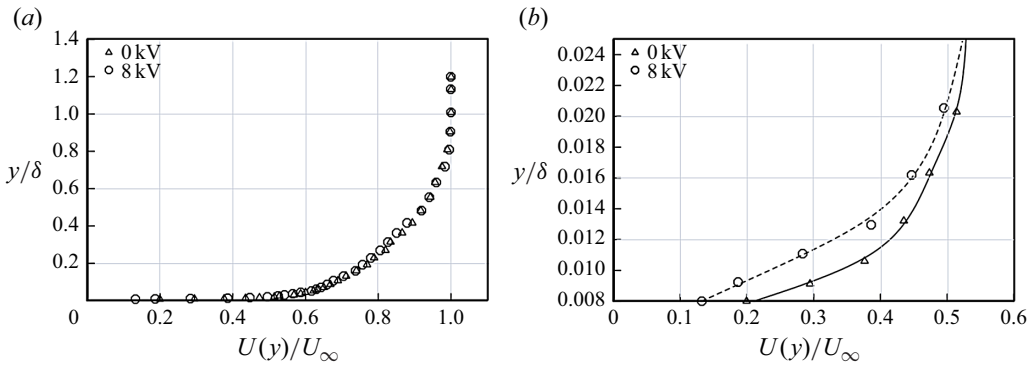


Figure 9. Mean velocity profiles for the baseline (0 kV) and spanwise sublayer blowing (8 kV) boundary layers across the layer (a) and with a magnified view near the wall (b) for the case with $Re_\theta = 4760$.

an upward shift of the mean velocity profiles when scaled by inner variables. The solid line corresponds to the log region for the baseline boundary layers in figure 5. Additionally, the slope of the log layer is also affected by the spanwise buffer layer blowing. This effectively changes the von Kármán coefficient, which prevents the use of the Clauser method to determine the wall shear stress from the mean velocity profiles of the actuated boundary layers. As a result, with the spanwise blowing cases the wall shear stress was determined from the drag measuring platen.

Further evidence of the effect of the spanwise buffer layer blowing on the mean velocity profiles is shown in figure 9. This compares the outer-variable scaled mean velocity profiles for the baseline (0 kV) and spanwise buffer layer blowing (8 kV) boundary layers at the lowest $Re_\theta = 4760$, where the boundary layer thickness was sufficient to allow hot-wire measurements close to the wall. Figure 9(a) shows profiles to the full extent of the boundary layer. The portion of the profile closest to the wall is shown in figure 9(b). It is evident when normalized by outer variables, that the effect of the spanwise buffer layer blowing is primarily confined to the near-wall region. There, it has resulted in a reduction in the near-wall mean strain rate that is consistent with a lowering of the wall shear velocity.

The drag reduction indicated by the force balance was also verified by comparison of the TBL momentum thicknesses measured directly upstream and downstream of the actuator platen. This was performed for the case at $Re_\theta = 4760$ that was shown in figure 9. Mean velocity profiles from that case were input to the appropriate form of the momentum integral equation to verify that the reduction of wall shear stress was consistent with that measured directly from the drag measurement platen, which recorded for this case a 71 % drag reduction. This level of drag reduction corresponds to a reduction in friction velocity of $u_{\tau_{plasma}}/u_{\tau_{baseline}} = 0.54$. Measurement of the momentum and displacement thicknesses just upstream of the actuator platen gave $\theta = 5.4$ and $\delta^* = 7.2$ mm for a shape factor of $H = 1.33$. The corresponding values just downstream of the platen were $\theta = 5.5$ and $\delta^* = 7.6$ mm for a shape factor of $H = 1.38$. Application these momentum thickness values to the appropriate form of the Kármán momentum integral equation produced a value of $u_{\tau_{plasma}} = 0.37 \text{ m s}^{-1}$. As indicated in table 1, in the lowest Reynolds number case, $u_{\tau_{baseline}} = 0.67 \text{ m s}^{-1}$. It then follows that based on the integral momentum balance, $u_{\tau_{plasma}}/u_{\tau_{baseline}} = 0.37 \text{ (m s}^{-1})/0.67 \text{ (m s}^{-1}) = 0.54$, which is in perfect agreement with the value measured from the force balance. Again we note that Jasinski & Corke (2020) using the same force balance with a smooth platen surface matched the Coles–Fernholz relation (Baars *et al.* 2016) to within 1 % over a wide range of Re_θ .

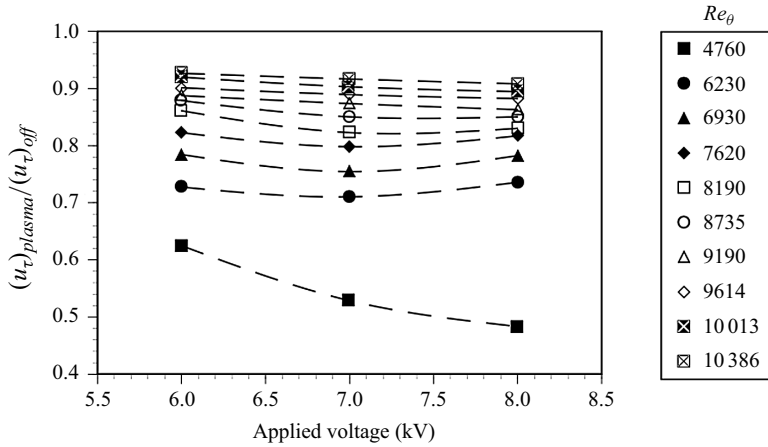


Figure 10. Ratio of wall shear velocities with buffer layer blowing on and off for different actuator voltages and momentum thickness Reynolds numbers.

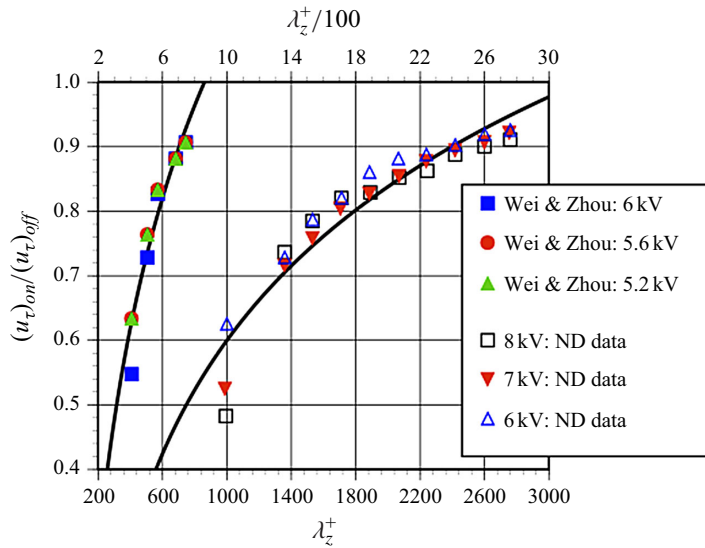


Figure 11. Ratio of wall shear velocities with buffer layer blowing on and off from figure 10 along with data from Wei & Zhou (2024) shown as a function of the actuator electrode spacing scaled by inner variables. Line is a logarithmic fit.

Figure 10 documents the change in the wall shear velocity as a function of the pulsed-DC voltage for each of the boundary layers at the different momentum thickness Reynolds numbers. At the higher Reynolds numbers, the trend was a general lowering of shear velocity with increasing actuator voltage. However, at several of the lower Reynolds numbers, the highest actuator voltage causes the shear velocity to increase above a minimum. For our cases, this trend begins to occur for $Re_\theta \leq 8735$. Reviewing the values of \bar{W}_{max}/u_τ in table 2, which are representative of the 8 kV actuator voltage, would suggest that an optimum condition that minimizes τ_w might be where the scaled spanwise blowing is $\bar{W}_{max}/u_\tau \approx 0.5$.

The magnitude of the spanwise blowing is, however, not the only design parameter that affects the change in the wall shear stress. The other is the spanwise spacing between the

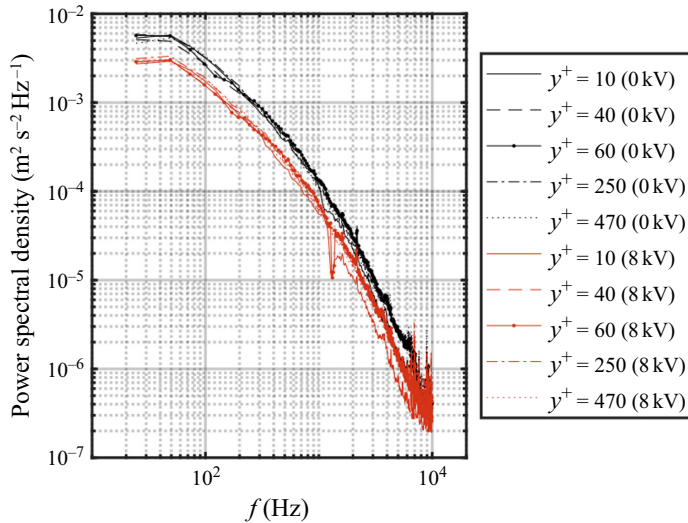


Figure 12. Power spectral density of streamwise velocity fluctuations at different heights in the boundary layer at $Re_\theta = 4760$ without and with buffer layer blowing.

pulsed-DC actuator electrodes, that are ‘blowing sites’ which determines the number of low-speed streaks under simultaneous control. This is illustrated in figure 11 which replots the change in the wall shear velocity from figure 10 now as a function of the spanwise spacing in inner variables, λ_z^+ , between the actuator electrodes (indicated by the ND data). This is observed to collapse all of the data onto a single curve suggesting that λ_z^+ is a primary scaling parameter for the spanwise blowing effect on u_τ . The line is a logarithmic fit to the results. The top abscissa corresponds to the actuator array electrode spacing divided by 100, which is the average spanwise wavelength of the near-wall streak structure observed by Kline *et al.* (1967). Thus, the upper abscissa can be read as being the number of near-wall streaks between electrodes. Based on this, figure 11 indicates that the reduction in u_τ increases as the number of low-speed streaks contained in the interelectrode spacing (i.e. blowing sites) decreases. The curve fit indicates that the degree to which u_τ is reduced by the spanwise blowing scales logarithmically with the spacing between the electrodes, i.e. blowing sites. This logarithmic variation implies that the reduction in u_τ due to the actuation is inversely proportional to the spanwise interelectrode spacing.

As a precursor to the next section that focuses on the effects of the spanwise buffer layer blowing on the unsteady characteristics of the TBLs, figure 12 shows spectra of streamwise velocity fluctuations measured at different heights in the boundary layers without and with the buffer layer blowing for the case with $Re_\theta = 4760$. Comparing the spectra, they reveal that an effect was to uniformly lower the streamwise velocity fluctuations throughout the buffer and log layers. This reduction will later be correlated with a reduction in the turbulence production that results from the buffer layer blowing.

In comparing the spectra with and without the spanwise blowing, we also note that there is no evidence of a peak at the plasma actuator DC pulsing frequency (500 Hz) or its harmonics. This reveals two aspects. The first is that the flow does not sense any unsteadiness in the velocity induced by the DC pulsing. The second is that any electronic noise produced by the plasma actuator is too low to be detectable in generally sensitive hot-wire signals. The spurious downward spike in the spectra at approximately 1300 Hz only occurred at the spectra at the lowest sensor location at this lowest Reynolds number, and did not appear at any of the higher Re_θ cases.

3.1.1. Actuator scaling

In recent experiments, Cheng *et al.* (2021) and Wei & Zhou (2024) utilized a wall-mounted array of dielectric-barrier-discharge plasma actuators that followed our approach of generating a near-wall spanwise flow. The actuator arrangement followed our designs that were shown in figures 2 and 3, with the exception that rather than the unidirectional blowing illustrated in figure 2, they utilized a spanwise-opposed wall jet configuration that we have also utilized (Duong 2019; Thomas *et al.* 2019, 2023) and have shown to also be effective in lowering the viscous drag. Another difference is that they operated the plasma actuators with an AC waveform rather than in our case, a pulsed-DC waveform, with the latter being more energy efficient.

As in our experiments, Cheng *et al.* (2021) and Wei & Zhou (2024) performed direct drag measurements using a floating-element force balance having a 20 cm^2 platen area. The platen was located just downstream of the plasma actuator array. In the Wei & Zhou (2024) experiments, $520 \leq Re_\tau \leq 747$, which are considerably lower than our range of Re_τ values with $2489 \leq Re_\tau \leq 4810$.

As in our experiments shown in figure 10, Cheng *et al.* (2021) and Wei & Zhou (2024) investigated the effect of the plasma actuator voltage (E_{p-p} in their case) on the friction drag reduction. They found there to be an optimum voltage that was a function of Re_τ , similar to our case put in terms of Re_θ in figure 10. At their optimum power levels, the viscous drag reduction they obtained ranged from 20 % to 75 % which is comparable to the present results (indicated by the ND data) shown in figure 11, which is expressed in terms of the viscous shear velocity, u_τ .

Cheng *et al.* (2021) documented an increase in the von Kármán coefficient that we previously documented in figure 8. Other documented characteristics noted by Cheng *et al.* (2021) were a reduction in the $[u, v]$ Reynolds stress and turbulence energy production that accompanied the drag reduction that has been previously documented by Duong (2019) and Duong, Corke & Thomas (2021). They similarly obtained ensemble-averaged streamwise velocity fluctuation time series based on a ‘variable-interval time-averaged’ (VITA) detection in which they observed a reduction in the ‘ejection’ portion of the VITA signature that accompanied the spanwise blowing, also first documented by Duong (2019) and Duong *et al.* (2021).

Following these similar results, the large difference in the range of Re_τ between those (Cheng *et al.* 2021; Wei & Zhou 2024) and the present experiments offers an opportunity to further investigate the actuator scaling relations. With that objective, figure 11 also presents data from Wei & Zhou (2024) figure 2(a) of the change in the viscous drag as a function of Re_τ (expressed here as the ratio of the shear velocity with the actuator on and off) for their highest plasma actuator voltage, $E_{p-p} = 5.6$ and 6 kV. For their fixed physical spacing of the electrodes, the different Re_τ values resulted in different effective electrode spacing when normalized by inner variables, λ_z^+ . This is represented in figure 11 along with a logarithmic fit to their data. Again, the logarithmic variation with λ_z^+ shows that the reduction in friction drag is inversely proportional to the number of low-speed streaks under simultaneous control.

The data in figure 11 are cross-plotted in figure 13. In order to account for the difference between the opposed wall jets used in Wei & Zhou (2024) and the unidirectional wall jets used in the present study, the effective gap width used for opposed wall jets is taken as the distance from the surface electrode to the centre of the interelectrode gap (which forms a stagnation point for the opposed wall jets). In figure 13 the two sets of data representing the level of viscous drag reduction for two disparate ranges of shear-stress Reynolds numbers, collapse reasonably when the inner variable electrode spacing, λ_z^+ , is normalized by their respective baseline Re_τ values. As indicated, this normalization is

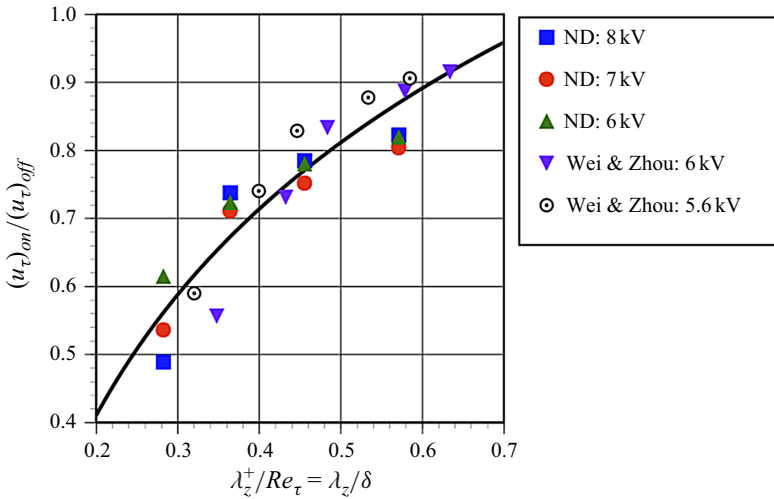


Figure 13. Cross-plot of data from Wei & Zhou (2024) and the present results (ND) shown in figure 11 with the inner variable electrode spacing of each scaled by their respective boundary layer baseline Re_τ values.

equivalent to normalizing the effective interelectrode spacing, λ_z , by the TBL thickness, δ . This provides strong evidence that the underlying mechanism of drag reduction is the same in both experiments and is dominated by the spanwise, plasma-induced blowing.

Thomas *et al.* (2019) had shown a linear relation between the reduction in the viscous drag and the buffer layer maximum blowing velocity, \overline{W}_{max} . In experiments similar to those that produced the results presented in figure 7, Thomas *et al.* (2019) (their figure 17) determined the plasma-induced velocity as a function of the applied pulsed-DC voltage. The induced velocities ranged from 0.40 to 1.6 m s^{-1} . In contrast, Wei & Zhou (2024) reported having plasma actuator generated velocities with a considerably larger range of 0.01–6.87 m s^{-1} . With that, they determined that for a given baseline boundary layer Re_τ , the viscous drag reduction actually varied logarithmically with the actuator blowing velocity, \overline{W}_{max} .

This difference in the actuator blowing velocity between those of Wei & Zhou (2024), and those cited by Thomas *et al.* (2019), which are the same for the results presented in this section and listed in table 2, provided another means to investigate actuator scaling. This is embodied in figure 14 in which the data from Wei & Zhou (2024) are replotted for their highest actuator voltage, $E_{p-p} = 6 \text{ kV}$, with the highest blowing velocity, $W_{max} = 6.87 \text{ m s}^{-1}$, at their two highest Re_τ values. Included in the plot are the data from the present study (figure 10) at the two pulsed-DC actuator voltages of 7 and 8 kV for the two lowest Re_τ cases. Despite the approximate order of magnitude lower actuator blowing velocity, and five-times larger Re_τ used in the current study, a comparable reduction in u_τ is produced. The logarithmic trend of the viscous drag reduction documented by Wei & Zhou (2024) is readily apparent in the plot. The present data in figure 10 are highlighted by the dashed ovals. They are observed to fall on the Wei & Zhou (2024) trends when the actuator blowing velocity in inner variables, W_{max}^+ , on the abscissa is scaled by the corresponding Re_τ . This scaling is equivalent to a spanwise blowing velocity Reynolds number, $W_{max}\delta/\nu$.

Comparisons like these are extremely important not only in the application of this technology, but also in further understanding the flow physics underlying TBLs. Additionally, the two different types of plasma actuators (unidirectional or opposed blowing) used in these studies represents alternate methodologies to produce the spanwise

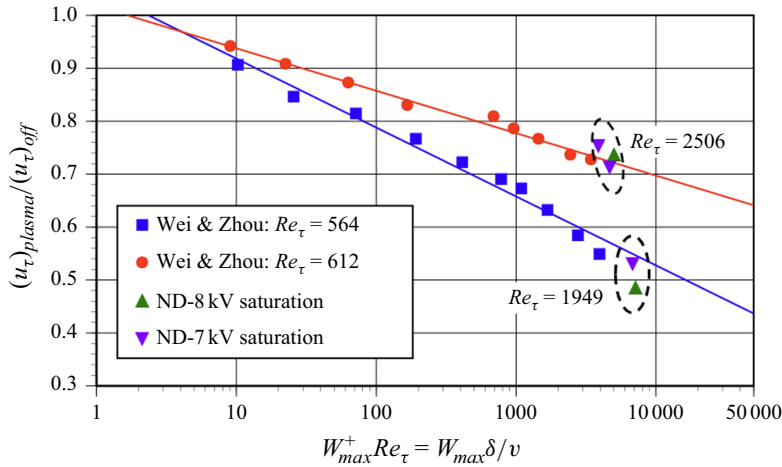


Figure 14. Cross-plot of data from Wei & Zhou (2024) that documented the effect on actuator blowing velocity on their viscous drag reduction, and corresponding data from figure 10 at two pulsed-DC voltages.

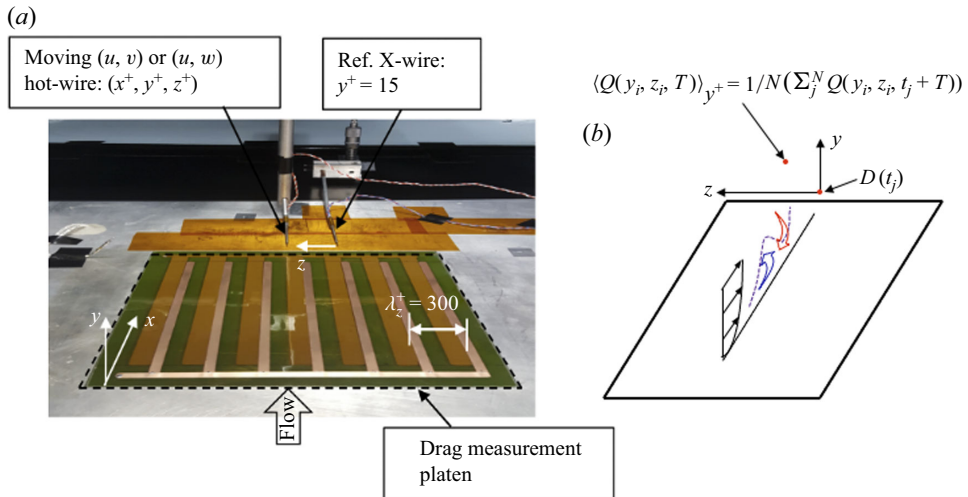


Figure 15. Photograph showing plasma actuator array mounted onto the surface of the drag measurement platen, and pair of X hot-wire probes (a) and coordinate for conditioned spatial velocity reconstructions (b).

buffer layer blowing. Knowing the scaling with Reynolds number and blowing velocity, opens the opportunity for other approaches such as compressed air tangential jets investigated by Zhang *et al.* (2024).

3.2. Unsteady boundary layer characteristics

This section documents changes in the structural characteristics of the TBL that result from the unidirectional spanwise buffer layer blowing. These experiments were performed in the Mach 0.15 Wind Tunnel with the TBL conditions given in table 1. The experimental set-up for these measurements is shown in figure 15.

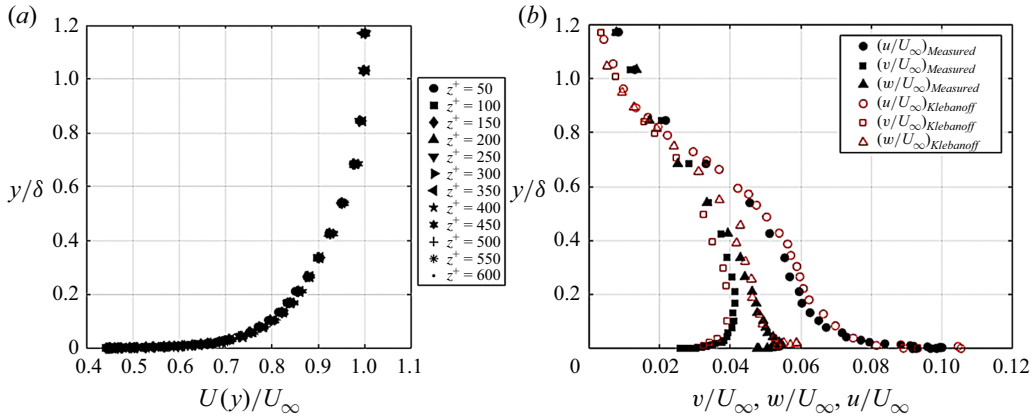


Figure 16. (a) Mean velocity profiles at different spanwise locations in the measurement region for the baseline TBL and (b) comparison of the u , v and w component turbulence intensity profiles measured at the $z^+ = 50$ to those of Klebanoff (1954).

The actuator array in this set-up was fabricated in the same manner as previously discussed in § 2. However, in this set-up, the actuator array consisted of seven plasma actuators spaced 28 mm apart compared with nine actuators spaced 22 mm apart in the Mach 0.6 wind tunnel experiments presented in § 3.1. Based on the u_τ value for the baseline boundary layer, the 28 mm electrode spacing corresponds to a $\lambda_z^+ \approx 300$. Based on figure 11, we anticipated that this would result in a sizable reduction in the wall shear stress that would produce tangible changes in the characteristics of the turbulent boundary that could aid in identifying the underlying viscous drag reduction mechanisms.

The set-up included two dual hot-wire sensor probes. One $[u, v]$ dual-sensor hot-wire was fixed in space at a location that was 1 cm, or $x^+ = 115$ downstream of the actuator array. Previous measurements (Duong 2019; Duong *et al.* 2021) indicated that conditions there were representative of those over the plasma array. The spanwise location of the fixed sensor was aligned with the edge of an exposed electrode facing the covered electrode of one of the plasma actuators in the array. This spanwise location of the fixed $[u, v]$ sensor is defined as $z = 0$. The wall-normal position of the fixed $[u, v]$ sensor corresponded to $y^+ = 15$.

The second sensor involved interchangeable $[u, v]$ and $[u, w]$ dual-sensor hot-wires that were mounted to a traversing mechanism and moved in 3-D space throughout the boundary layer. The motion resolution of the traversing mechanism in each direction was $\Delta_z = 0.0254$ mm, which when normalized by TBL inner wall variables corresponded to $\Delta_z u_\tau / \nu = 0.27$. All of the hot-wires were operated in a constant temperature mode using the previously described floating ground design.

Figure 16(a) documents the spanwise uniformity of the baseline boundary layer mean velocity profile measured 1 cm downstream of the passive plasma actuator array. The profiles were measured at spanwise locations in $z^+ = 50$ intervals over a range of $z^+ = 600$. This physically corresponded to a span of 5.22 cm in increments of 4.25 mm that encompassed a pair of plasma actuator electrodes in the array. A comparable spanwise uniformity occurred for the u , v and w turbulence intensity profiles (Meyers 2023). Figure 16(b) compares the baseline u , v and w component turbulence intensity profiles with those of Klebanoff (1954). While these profiles are for the baseline boundary layer, as documented by Meyers (2023), similar spanwise uniformity existed for the boundary layer with the spanwise buffer layer blowing.

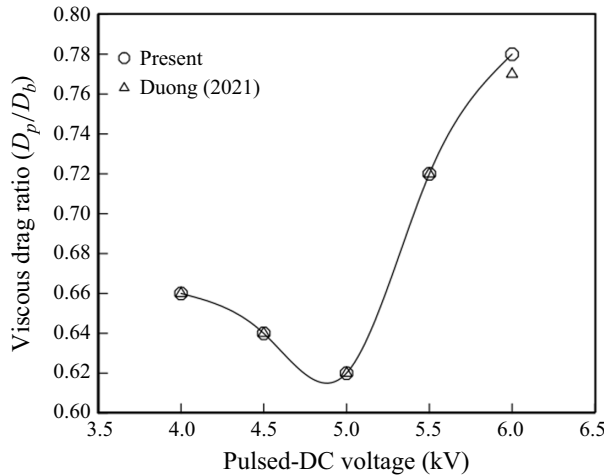


Figure 17. Viscous drag reduction as a function of the Pulsed-DC actuator array DC voltage in experiments focusing on the unsteady TBL characteristics produced by spanwise buffer layer blowing.

In these experiments, it was necessary to first determine the operation settings for the plasma actuator array. The object was to find the condition that would provide the largest reduction in the wall shear stress, with the assumption that this would provide the best opportunity to examine the effect this had on the underlying structural characteristics of the boundary layer. For this, the DC pulsing frequency and duty cycle remained fixed at the original 500 Hz and 1 %, respectively. Only the DC voltage was varied.

The effect of varying the plasma actuator array DC voltage on the per cent of drag reduction is shown in figure 17. The plot includes results from the present experiment as well as from the previous experiment of Duong *et al.* (2021). The plasma actuator array had been rebuilt in the interim between the previous and current experiments and including the previous results provided an indication of the high degree of repeatability of the measurements. The agreement between the two experiments is shown to be excellent. A similar result for an opposed wall jet plasma actuator voltage that maximized the viscous drag reduction was documented by Cheng *et al.* (2021) (their figure 10).

As previously specified in § 2, the load cell for these experiments had a full-scale rating of 0.5 N (51 g) and a total uncertainty of 0.05 %, which equated to a force measurement uncertainty of 0.025 g. In this set of experiments, the time-averaged shear force exerted on the platen was obtained from a necessary number of records, each containing 30 s of contiguous load cell voltages, that were needed to reach a stable mean value. Based on the results in figure 17, the pulsed-DC actuator voltage used in this phase of the experiments was fixed at 5 kV.

The effect of the buffer layer spanwise blowing on the three fluctuating velocity components and Reynolds stresses is presented in figure 18. These correspond to the $z^+ = 50$ spanwise location. These document a significant reduction in the fluctuation levels and Reynolds stresses across a majority of the boundary layer. Cheng *et al.* (2021) found comparable reductions in the uv -Reynold stress that accompanied their viscous drag reduction. These results are particularly significant since these turbulent stress components are important in the turbulence production near the wall (Corino & Brodkey 1969).

Figure 18 established a reduction in the turbulent stress values through most of the boundary layer. In establishing the scaling with inner-wall variables, Duong (2019) and Duong *et al.* (2021) had demonstrated a relation between the reduction in the u component of turbulence intensity and the reduction in u_τ that occurs with the spanwise buffer

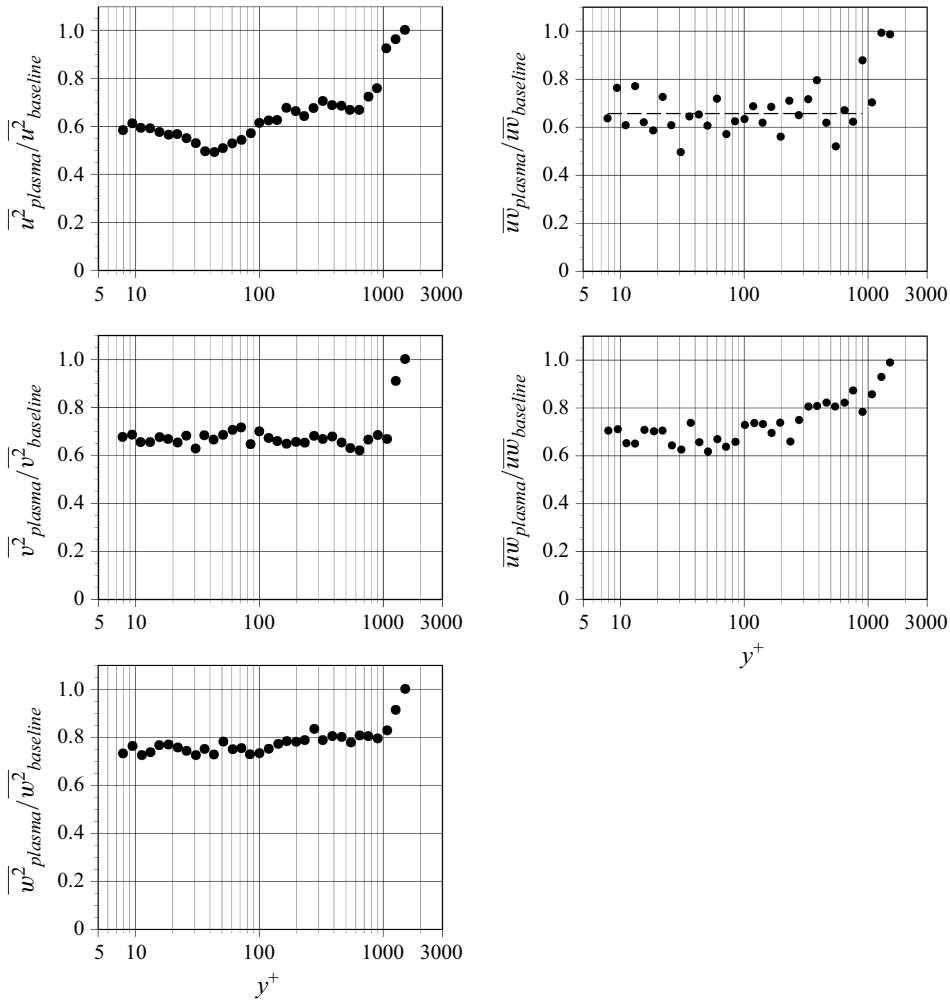


Figure 18. Wall-normal profiles of the buffer layer blowing to baseline ratios of the three fluctuating velocity components and Reynolds stresses measured at the $z^+ = 50$ location.

layer blowing. This involved defining a ratio $R_{u_i}^2$ where

$$R_{u_i}^2 = \frac{(\overline{u_i^2}/u_\tau^2)_{5\text{ kV}}}{(\overline{u_i^2}/u_\tau^2)_{0\text{ kV}}} \quad (3.1)$$

in which u_i refers to a fluctuating velocity component, u , v or w , and the subscripts 0 kV and 5 kV that, respectively, refer to the baseline and spanwise buffer layer blowing boundary layers. A similar approach was followed here in order to examine if the scaling applies to the v and w velocity components. For this, values of R_v^2 and R_w^2 were calculated at every height in the boundary layer at all of the spanwise locations. The result is shown in figures 19(a) and 19(b).

The R_v^2 and R_w^2 profiles are observed to reasonably collapse across the full z^+ span of the measurements. Spatially average values based on the region from the wall up to the edge of the log layer are indicated in each plot by the vertical dashed lines. The values are given in table 3. For reference, R_u^2 is also included in the table.

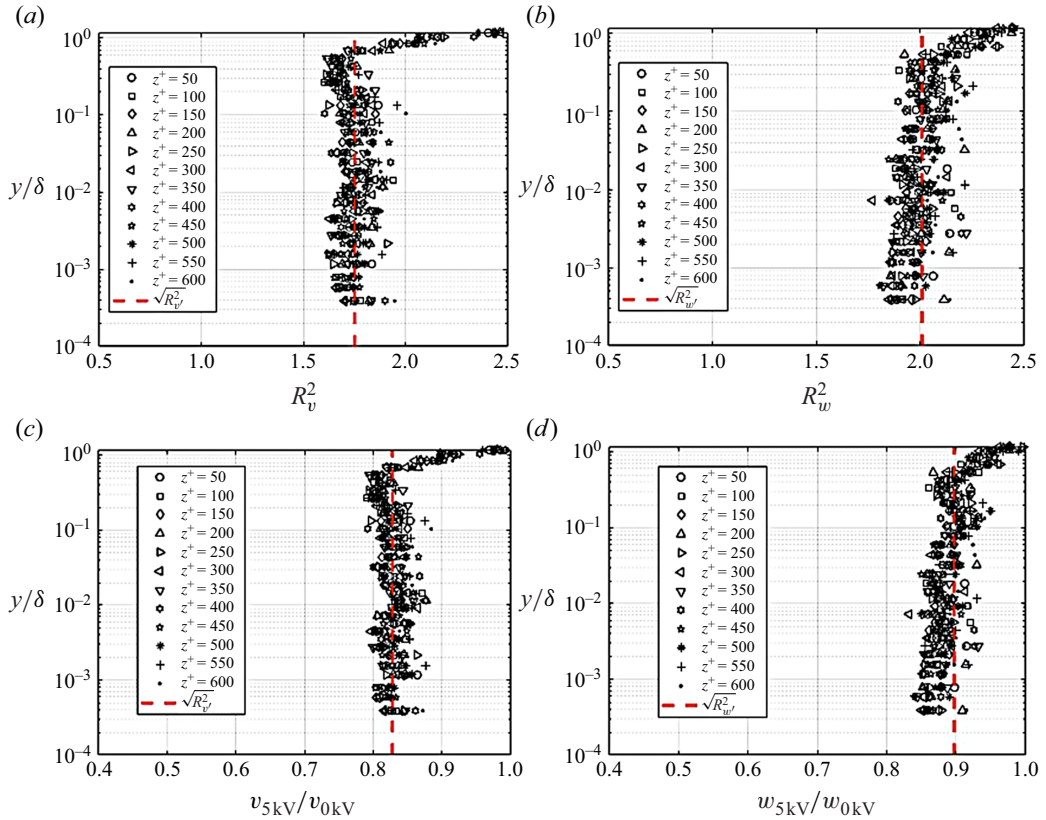


Figure 19. Wall-normal profiles of R_v^2 (a) and R_w^2 (b) given by (3.1), and wall-normal profiles of $v_{5\text{ kV}}/v_{0\text{ kV}}$ (c) and $w_{5\text{ kV}}/w_{0\text{ kV}}$ (d) at each measured spanwise position in the TBLs.

Quantity	u	v	w
Spatially averaged $R_{u_i}^2$	1.85	1.75	2.01
$\overline{u'_{i,5\text{ kV}}/u'_{i,0\text{ kV}}}$	0.85 (0.84)	0.81 (0.82)	0.90 (0.90)
$\overline{u'_{i,5\text{ kV}}/u'_{i,0\text{ kV}}} (\%)$	-18	-21	-13

Table 3. Turbulence intensity component scaling with u_τ .

Note: ' denotes RMS

Rewriting (3.1) as

$$R_{u_i}^2 = \left(\frac{u_{\tau,0\text{ kV}}}{u_{\tau,5\text{ kV}}} \right)^2 \overline{\left(\frac{u'_{i,5\text{ kV}}}{u'_{i,0\text{ kV}}} \right)^2} \quad (3.2)$$

separates out the ratio of the wall shear velocities for the baseline (0 kV) and buffer layer spanwise blowing (5 kV) cases. In the present experiment with the 5 kV actuator voltage

$$\left(\frac{u_{\tau,0\text{ kV}}}{u_{\tau,5\text{ kV}}} \right)^2 = 2.56 \quad (3.3)$$

so that

$$R_v^2 = 2.56 \overline{\left(\frac{v'_{5\text{kV}}}{v'_{0\text{kV}}} \right)^2} \quad \text{and} \quad R_w^2 = 2.56 \overline{\left(\frac{w'_{5\text{kV}}}{w'_{0\text{kV}}} \right)^2}. \quad (3.4)$$

The values of $\overline{u'_{i,5\text{kV}}/u'_{i,0\text{kV}}}$ that are needed to satisfy (3.4) are given without parentheses in table 3.

As a check, the wall-normal profiles of $v'_{5\text{kV}}/v'_{0\text{kV}}$ and $w'_{5\text{kV}}/w'_{0\text{kV}}$ at each spanwise position are shown in figures 19(c) and 19(d). As with the R_v^2 and R_w^2 profiles shown in the figure, a reasonable collapse is observed. The spatial average for each plot based on the region from the wall to the edge of the log layer is again shown by the vertical dashed line. These are indicated by the bracketed values in table 3. The excellent agreement between the predicted and actual values supports the relationship (3.1) of the levels all three components of the turbulence intensity to the level of the wall shear stress.

This scaling provides an indication of how the spanwise buffer layer blowing affects the individual turbulence components. The values of $u'_{5\text{kV}}/u'_{0\text{kV}}$, $v'_{5\text{kV}}/v'_{0\text{kV}}$ and $w'_{5\text{kV}}/w'_{0\text{kV}}$ are also given in table 3. These indicate that the largest effect of the spanwise buffer layer blowing is on the v' fluctuations with a 21 % reduction. This is closely followed by the u' fluctuations with a 18 % reduction, and finally the w' fluctuations with a 13 % reduction. Note that these values are the spatial average over the full boundary layer thickness. As shown in figure 18, the reduction in the peak velocity fluctuation levels with the buffer layer blowing are somewhat larger, and is greatest for the streamwise component.

As with Duong *et al.* (2018), the spanwise buffer layer blowing was found to result in a reduction in the turbulence production defined as

$$P = p \frac{\delta}{U_\infty^3} = -\overline{uv} \frac{dU}{dy} \frac{\delta}{U_\infty^3}. \quad (3.5)$$

This is documented in figure 20, which shows wall-normal profiles of the production based on (3.5) without and with buffer layer blowing. The decrease in the production with the buffer layer blowing was particularly pronounced near $y^+ = 12$, where an approximate 66 % reduction in the production occurs. Cheng *et al.* (2021) similarly documented a substantial reduction in the turbulence production, $-\overline{uv}(dU/dy)$, near the wall for their drag reduced cases, which they found to be ‘consistent with the stabilized streaks’.

3.2.1. Conditional flow field reconstruction

In order to further investigate the effect of the flow control on the coherent structures in the near-wall region of the boundary layer, conditional-averaged reconstructions of the flow field were performed. The coordinate system for this was shown in figure 15(b). With this, the $[u, v]$ hot-wire probe at the fixed $[x, z]$ location was again positioned at $y^+ = 15$. Recall that the fixed probe was located at $x^+ = 115$ downstream of the plasma actuator array, where previous results (Duong 2019; Duong *et al.* 2021) had indicated conditions were representative of those over the plasma array. The fixed probe provided the $[u, v]$ time series used to define ‘events’ on which the conditional averages were based. The other $[u, v]$ and $[u, w]$ hot-wire probes were located at the same x location as the fixed probe, and moved in the $[y, z]$ directions with the same range as used to compile results in figure 16. The time series from both the fixed and moving hot-wire probes were sampled simultaneously.

The method for defining an ‘event’ utilized the VITA technique that was pioneered by Blackwelder & Kaplan (1976). This utilized the u velocity time series and applied a

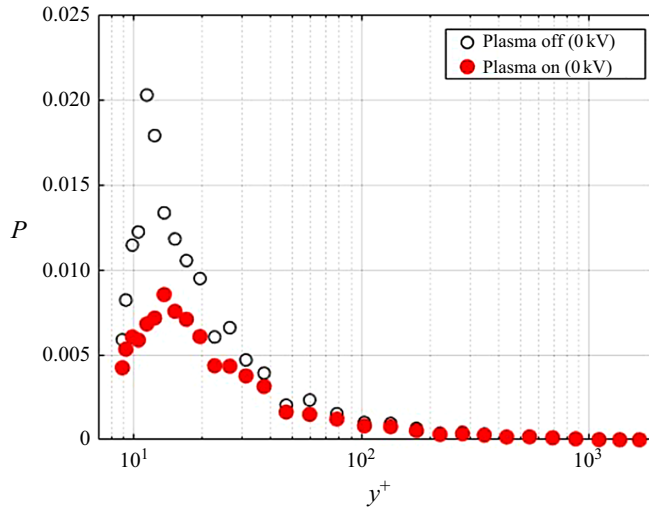


Figure 20. Comparison between wall-normal profiles of the turbulence production of the baseline and buffer layer blowing cases.

discriminator, D , such that

$$D(t) = \begin{cases} 1 & \text{if } \widehat{var} > ku_{rms}^2 \\ 0 & \text{Otherwise} \end{cases} \quad (3.6)$$

where

$$\widehat{var}(x_i, t, T) = \widehat{u}^2(x_i, t, T) - [\widehat{u}(x_i, t, T)]^2 \quad (3.7)$$

is the localized variance of streamwise velocity fluctuations over the time interval T at a spatial location, x_i . With this discriminator, Blackwelder & Kaplan (1976) recommended that $k = 1.2$, and that $Tu_\tau^2/\nu = 10$. Furthermore, they applied the detection at $y^+ = 15$ in the boundary layer, where the turbulence intensity was a maximum. The conditionally averaged velocity field that results from VITA detection is thought to embody the initial ‘ejection’ of low momentum fluid from the wall that is followed by a faster moving ‘sweep’ of fluid that approaches from outside the wall region (Blackwelder & Kaplan 1976). These motions are associated with streamwise near-wall vortices. Figure 21(a) shows examples of the streamwise velocity ‘signature’ associated with VITA detections having different values of the threshold parameter, k .

Once a reference time for each VITA event was determined by the detection function, $D(t)$, the characteristics of the flow field in time and space were constructed based on a conditional average defined as

$$\langle Q(y_i, z_i, T) \rangle_{y^+=15} = \frac{1}{N} \sum_j^N Q(y_i, z_i, t_j + T) \quad (3.8)$$

where Q is the estimated quantity which is a function of the independent variables $[y_i, z_i]$ that denote the position in space of the moving probe where the sampling occurred, and the subscript $y^+ = 15$ denotes the wall-normal position of the fixed probe where the detection occurred. The quantities t_j are those points in the time series when a detection occurred. Since $D(t)$ was equal to unity only during very short time intervals, the times, t , were taken to be midway between the beginning and end of the period during which $D(t) \neq 0$.

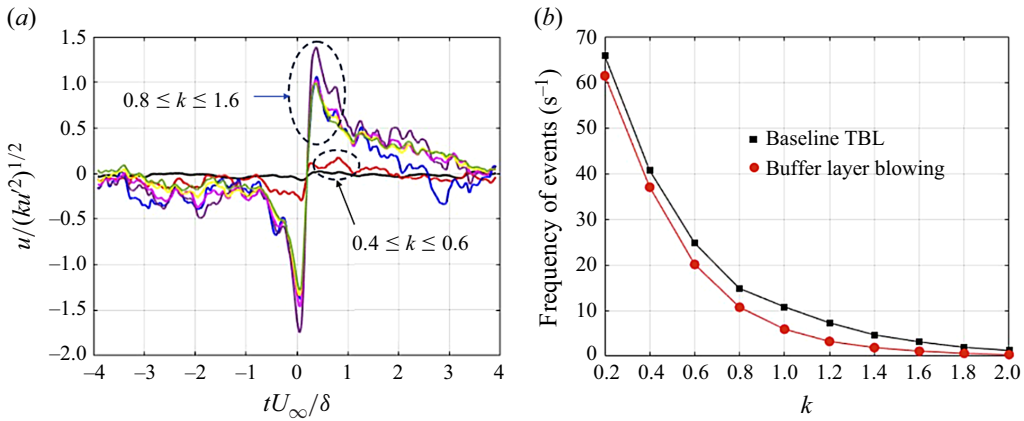


Figure 21. Sample ensemble averages for different VITA threshold parameters, k , in baseline boundary layer (a) and variation in the frequency of VITA events as a function of k , for the baseline and spanwise buffer layer blowing TBLs (b). Here $k = 1.2$ used for conditional measurements.

A positive or negative time delay T with a range of $-4 \leq T^* = (TU_\infty/\delta) \leq 4$, was used to determine the temporal behaviour of Q before and after a detection occurred. Here N is the total number of samples used to form the ensemble average.

One of the issues in comparing ensemble averages based on the occurrence of VITA ‘ejection-sweep’ events is that as previously documented (Duong 2019; Duong *et al.* 2021), the number and strength of these events is significantly reduced with the spanwise buffer layer blowing. This is demonstrated in figure 21(b) which shows the frequency of events as a function of the VITA threshold parameter, k , for the baseline and spanwise buffer layer blowing boundary layers. The frequency of events was simply defined as the inverse of the number of VITA detections that occurred over the same fixed period of time. This demonstrates that at any value of the detection threshold parameter, k , the frequency of events was significantly lower in the boundary layer with the buffer layer blowing. At the recommended (Blackwelder & Kaplan 1976) $k = 1.2$ with buffer layer blowing, the frequency of VITA events was approximately 57 % lower than with the baseline boundary layer. This reduction in the frequency of VITA events with buffer layer blowing is quite comparable to the 62 % reduction in the viscous drag and the 38 % reduction in u_τ that had occurred with the buffer layer blowing. Such a connection between the wall shear velocity and frequency of ejection-sweep events was first reported by Kline *et al.* (1967).

The relevance of the VITA events to the turbulence Reynolds stresses and thereby turbulence production (3.1), is illustrated in figure 22. This shows ensemble averaged time series of the $[uv]$ - and $[uw]$ -Reynolds stress associated with VITA events measured at $y^+ = 15$ for the baseline and spanwise buffer layer blowing boundary layers. The threshold parameter for these was $k = 1.2$. These time series indicate a substantial reduction in both Reynold stress components during ‘ejection-sweep’ events that results from the spanwise blowing. Thus, in addition to reducing the frequency of these events, when they do occur their contribution to the turbulence production is substantially reduced. Overall, due to the spanwise buffer layer blowing, the uv -stress component associated with ‘ejection’ and ‘sweep’ events was reduced by 52 % and 67 %, respectively. Similarly, the uw -stress was reduced by 32 %. In concurrence with these results, while applying the VITA technique Cheng *et al.* (2021) observed a reduction in the amplitude of the ‘ejection’ portion of the VITA ensemble velocity time trace.

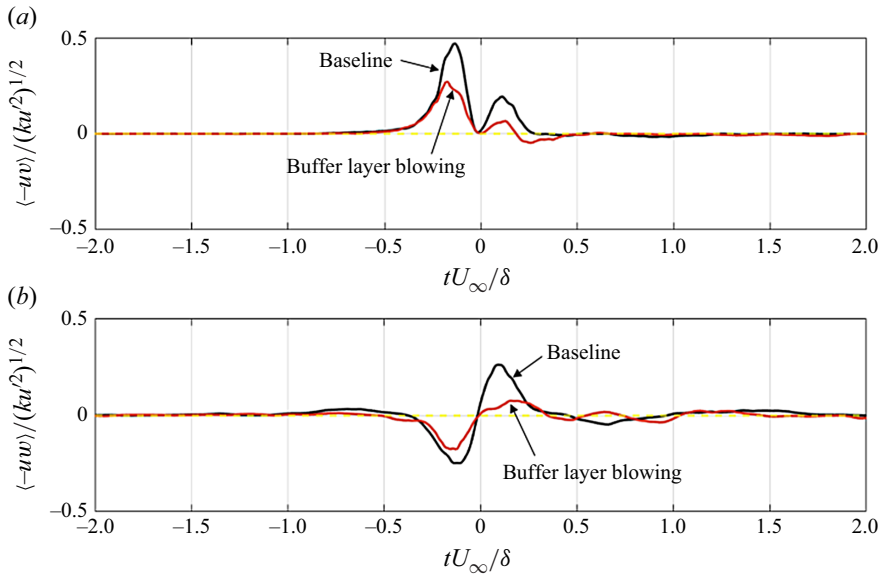


Figure 22. Conditionally averaged $\langle uv \rangle$ and $\langle uw \rangle$ Reynolds stress time traces associated with VITA detections measured at $y^+ = 15$ for baseline and spanwise buffer layer blowing boundary layers.

3.2.2. Coherent vortical structure reconstructions

Three-dimensional reconstructions of vortical structures were obtained through ensemble averages of the velocity field in 3-D space that were correlated to the occurrence of VITA events. The time series used in the VITA detection was from the u -component of the stationary hot-wire located 1 cm downstream of the actuator array at a height corresponding to $y^+ = 15$. The spanwise position corresponded to $z = 0$ shown in figure 15. The reconstructed velocity field was obtained from the (u, v) and (u, w) hot-wire sensors that were moved in the (y, z) directions at a fixed x position located 1 cm downstream of the actuator array. Velocity time series from the stationary hot-wire probe and either of the dual sensor probes were simultaneously sampled. In postprocessing, the time instants of a VITA detection in the u -velocity from the stationary probe was used to mark a time instant in the (u, v) or (u, w) time series about which an ensemble average was constructed.

An important step in the spatial velocity reconstructions was determining the spanwise extent to which the velocity fluctuations at the location of the movable probe were correlated with the VITA events at $z = 0$. The result is presented for the baseline boundary layer in figure 23. This documents the correlation coefficient, $\bar{R}_{max} = \sigma[u(z_{ref}^+, t)u(z^+, t + \tau)]/(\sigma[u(z_{ref}^+)]\sigma[u(z^+)])$, between velocity time series of the fixed hot-wire sensor and that of a second sensor spaced some spanwise distance, z , apart. Here σ is the standard deviation. The two sensors were at the same height in the boundary layer, and based on the definition $-1 \leq \bar{R} \leq +1$.

Figure 23 indicates that velocity fluctuations associated with VITA events detected at $z = 0$ ($z^+ = 0$) are reasonably correlated with velocity fluctuations to a spanwise distance corresponding to $z^+ = 400$. This was then taken as the spanwise limit over which spatial velocity reconstructions were performed.

Figure 24 presents constant level contours of the wall-normal vorticity in the $[x^+, z^+]$ plane at a height of $y^+ = 15$, based on the conditionally averaged velocity field correlated with $k = 1.2$ VITA events detected at $[x^+, y^+, z^+] = [0, 15, 0]$, namely

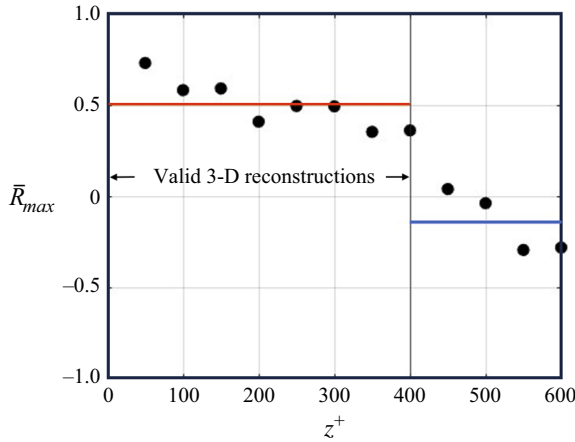


Figure 23. Spanwise correlation coefficient, $[\bar{R}(z^+, \tau)]_{max}$, between the fixed probe at $[x^+, y^+, z^+] = [0, 15, 0]$ and the moving probe at $[x^+, y^+, z^+] = [0, 15, 50-600]$ in baseline boundary layer.

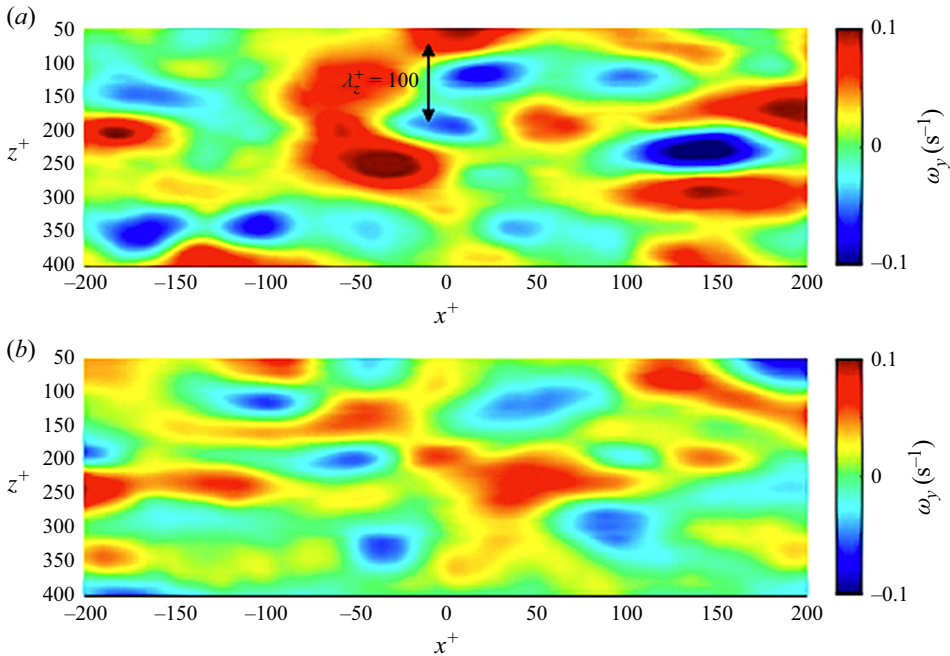


Figure 24. Constant level contours of $\langle \omega_y(y_{15}^+, z_i^+, x_i^+) \rangle_{[x^+, y^+, z^+] = [0, 15, 0]}$ for the baseline (a) and spanwise sublayer blowing (b) boundary layers.

$\langle \omega_y(y_{15}^+, z_i^+, x_i^+) \rangle_{[x^+, y^+, z^+] = [0, 15, 0]}$. Figure 24(a) is for the baseline boundary layer, and the figure 24(b) is for the boundary layer with spanwise buffer layer blowing. For these plots and those to follow, the original correlation time scale was converted to a pseudospacial streamwise length scale, x^+ , by assuming a convection speed of $0.6U_\infty$.

The coherent features of ω_y in the baseline boundary layer are consistent with the spanwise mean flow inhomogeneity caused by the counter-rotating longitudinal vortical structures associated with the wall ‘streak structure’ first observed by Kline *et al.* (1967).

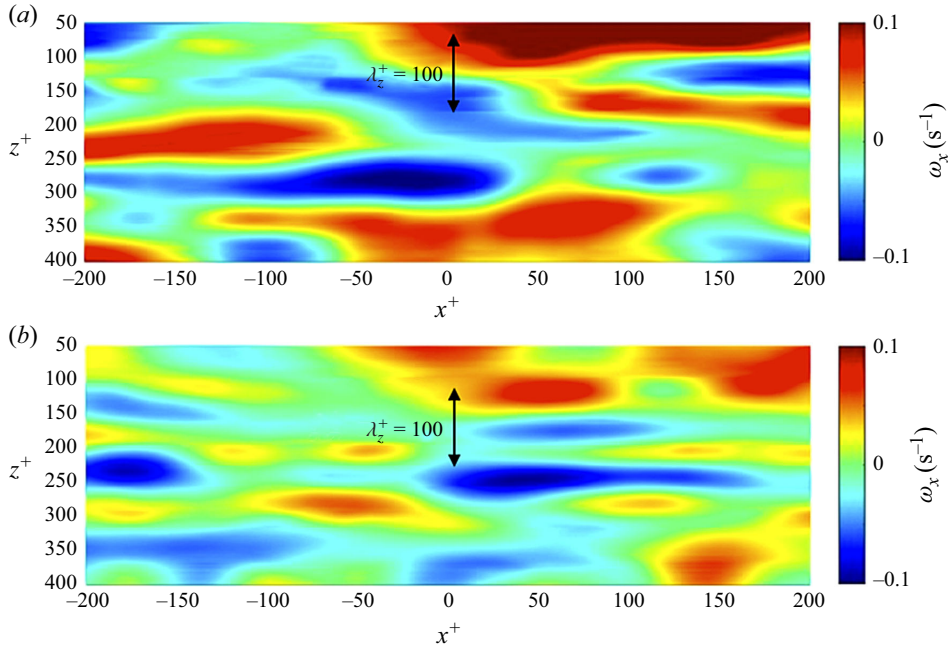


Figure 25. Constant level contours of $\langle \omega_x(y_{15}^+, z_i^+, x_i^+) \rangle_{[x^+, y^+, z^+] = [0, 15, 0]}$, for the baseline (a) and spanwise sublayer blowing (b) boundary layers.

The spanwise spacing between ω_y contours of opposite signs, for example denoted in [figure 24\(a\)](#), is consistent with the well documented $\lambda_z^+ = 100$ streak spacing.

As previously discussed, our spanwise sublayer blowing approach was initially motivated in part, by the channel flow simulations of Schoppa & Hussain (1998) who found it resulted in a reduction in the spanwise mean flow distortion that flanked the low-speed wall streak structure, as well as to produce a significant reduction in the wall shear stress. Schoppa & Hussain (2002) later linked these observations to the control of ‘streak transient growth’ in which the wall normal vorticity, ω_y , is a critical stability parameter. The premise was that this form of flow control would weaken ω_y and thereby intervene in the autonomous cycle shown in [figure 1](#).

[Figure 24](#) reveals that the spanwise buffer layer blowing has, in fact, significantly reduced the levels of ω_y . Specifically, when averaged over a 3-D region within $-250 \leq x^+ \leq 250$ by $0 \leq y^+ \leq 20$ by $0 \leq z^+ \leq 400$, the ω_y was reduced by 58 % compared with the boundary layer without the spanwise buffer layer blowing. This reduction in ω_y is nearly the same as the reduction in u_τ , which supports the connection observed by Schoppa & Hussain (1998). Consistent with the mechanism shown in [figure 1](#), the reduction in ω_y due to the spanwise blowing should result in weakened sublayer streamwise vorticity, ω_x , which is examined next.

The near-wall longitudinal vortical structures would appear as coherent features in the ω_x vorticity. This is presented in [figure 25](#) as constant level contours in the $[x^+, z^+]$ plane at a height of $y^+ = 15$, based on the conditionally averaged velocity field correlated with $k = 1.2$ VITA events detected at $[x^+, y^+, z^+] = [0, 15, 0]$, namely $\langle \omega_x(y_{15}^+, z_i^+, x_i^+) \rangle_{[x^+, y^+, z^+] = [0, 15, 0]}$. Similar to [figure 24](#), [figure 25\(a\)](#) is for the baseline boundary layer, and [figure 25\(b\)](#) is for the boundary layer with spanwise buffer layer blowing. The elongated near-wall vortical structures are readily apparent for the baseline

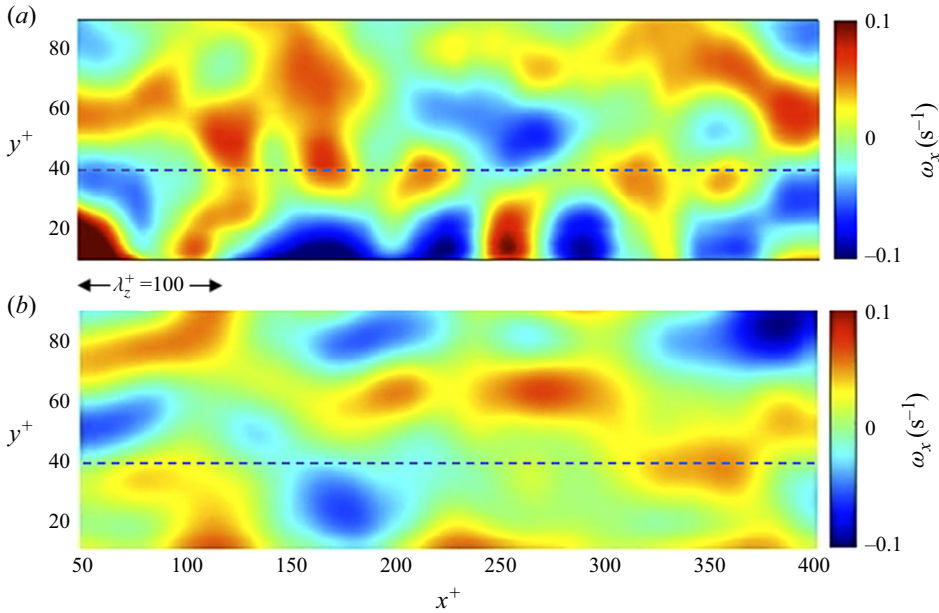


Figure 26. Constant level contours of $\langle \omega_x(x_0^+, y_i^+, z_i^+) \rangle_{[x^+, y^+, z^+] = [0, 15, 0]}$, for the baseline (a) and spanwise sublayer blowing (b) boundary layers.

boundary layer (figure 25a). Their spanwise spacing is again in agreement with the previously observed $\lambda_z^+ = 100$ streak spacing (Kline *et al.* 1967).

The spanwise buffer layer blowing has clearly reduced the overall magnitude of the streamwise vorticity in the elongated near-wall structures. In addition, it appears to have reduced the contiguous streamwise extent of these structures, which is related to VITA events of shorter duration and lower amplitude. However, when accounting for the lower u_τ levels that occur with the spanwise blowing, the average spanwise spacing between the elongated structures remains at $\lambda_z^+ = 100$ as indicated in figure 25(b).

To further illustrate the effect of the spanwise buffer layer blowing on the coherent near-wall longitudinal structures, figure 26 shows constant level contours in the $[y^+, z^+]$ (cross-flow) plane at the $x^+ = 0$ location, namely $\langle \omega_x(x_0^+, y_i^+, z_i^+) \rangle_{[x^+, y^+, z^+] = [0, 15, 0]}$. These again are based on the conditionally averaged velocity field that was correlated with the $k = 1.2$ VITA events detected at $[x^+, y^+, z^+] = [0, 15, 0]$. Similarly, figure 26(a) is for the baseline boundary layer, and figure 26(b) is for the boundary layer with spanwise buffer layer blowing.

This view through the near-wall region of the boundary layers represents a ‘cut’ in the $[y, z]$ -plane at $x^+ = 0$ (VITA detection location) of the constant level contours that were shown in figure 25. This cross-flow-plane view of the ω_x vorticity presents another realization of the counter-rotating vortex pairs that make up the near-wall longitudinal vortical structures. This view dramatically illustrates the effect of the spanwise buffer layer blowing to reduce the level of streamwise vorticity. As expected, this is particularly evident in the boundary layer sublayer ($y^+ \leq 40$) which is delineated by the dashed line in figure 26. This very significant reduction in sublayer streamwise vorticity is consistent with the observed reduction in ejection/sweep event Reynolds stress. Furthermore, it results in reduced transfer of high momentum fluid towards the wall which reduces the near-wall mean strain rate.

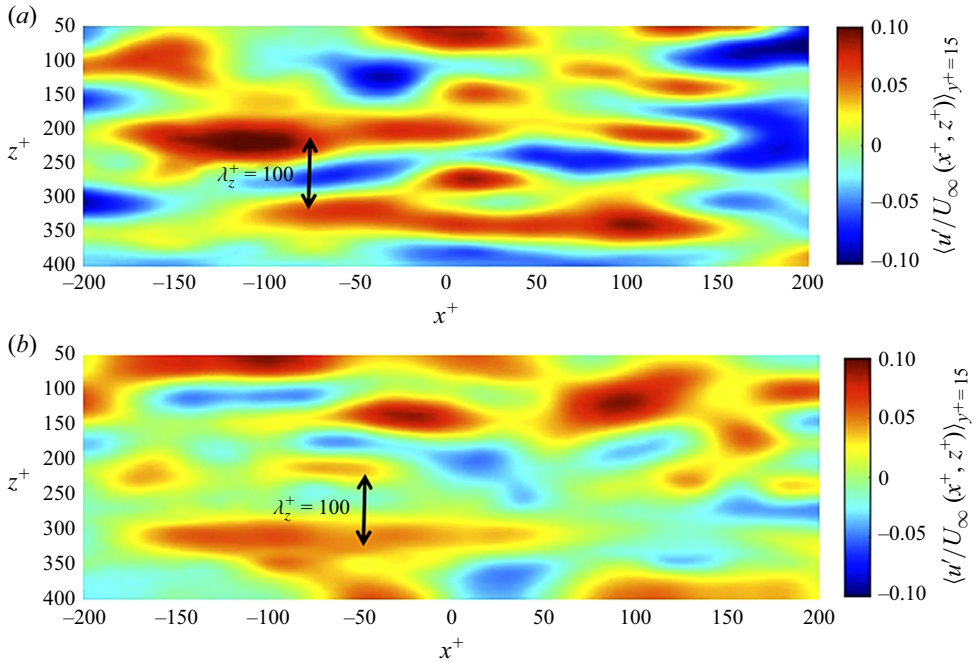


Figure 27. Constant level contours of $\langle u'/U_\infty(y_{15}^+, z_i^+, x_i^+) \rangle_{[x^+, y^+, z^+]=[0, 15, 0]}$, for the baseline (a) and spanwise sublayer blowing (b) boundary layers.

Figure 27 presents constant level contours of normalized streamwise velocity fluctuations in the top-down (x^+, z^+) plane at a wall-normal height of $y^+ = 15$ namely $\langle u'/U_\infty(y_{15}^+, z_i^+, x_i^+) \rangle_{[x^+, y^+, z^+]=[0, 15, 0]}$. Figure 27(a) is for the baseline flow and figure 27(b) is for the case of plasma-induced near-wall spanwise blowing. The elongated streaks that are present maintain the streak spacing of $\lambda_z = 100$ as expected in both the baseline and drag reduced cases. However, the level of streamwise velocity fluctuations is shown to be significantly reduced for the actuated case. This lower streamwise fluctuation level in the actuated case is a direct consequence of the suppression of near-wall streamwise vorticity produced by the spanwise blowing shown previously in figures 25 and 26.

3.3. Temporal recovery from spanwise buffer layer blowing

The ability to alter the TBL characteristics with on-demand spanwise buffer layer blowing provided an opportunity to investigate the characteristic time scales associated with turbulence production that could be documented when the boundary layer was allowed to return to its baseline condition. The approach then was to start from a state produced by the buffer layer blowing with boundary layer characteristics documented in the previous section, and then to follow the temporal development of the boundary layer characteristics following termination of the buffer layer blowing.

The experimental set-up to accomplish this is shown in figure 28. This utilized a timing circuit that after operating the pulsed-DC plasma actuators to produce the spanwise buffer layer blowing for 10 s, corresponding to a $t_1^+ = 18\,525$, then terminated the actuator operation. The voltage time series from the hot-wire sensors and load cell were recorded at the start of the process and continued for an additional 20 s, corresponding to a $t_2^+ = 37\,050$, which was found to be sufficient for the boundary layer conditions (mean

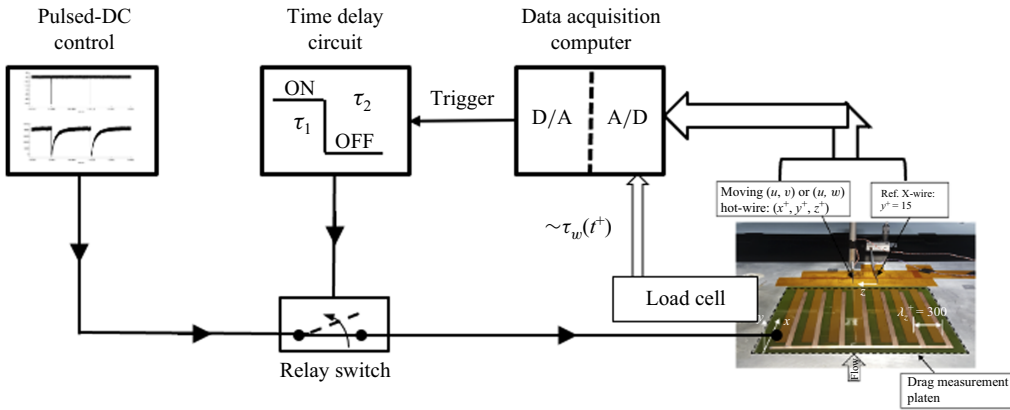


Figure 28. Schematic of the experimental set-up used in document the temporal effect of terminating the spanwise buffer layer blowing and boundary layer development to its baseline condition.

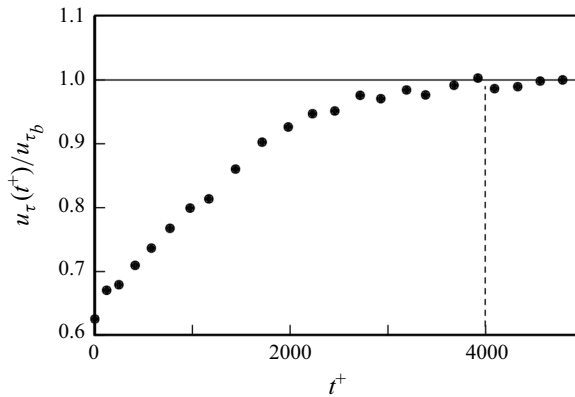


Figure 29. Temporal evolution of the ratio of the boundary layer wall friction velocity, $u_\tau(t^+)/u_{\tau_b}$, following the termination of the spanwise buffer layer blowing.

and fluctuating) to return to an asymptotic baseline state. This process was repeated until converged statistics were achieved.

The temporal evolution of several of the TBL characteristics back to their baseline state are presented in subsequent figures. In these, the time, t , following termination of spanwise blowing has been normalized using inner-wall variables. It is important to point out that the values of t^+ utilize the instantaneous $\tau_w(t^+)$ values that were recorded with the drag measuring platen, and which change as the boundary layer returns to its baseline state. In these figures, the subscript ‘b’ refer to the ‘baseline’ condition.

Figure 29 shows the temporal evolution of the ratio of the boundary friction velocity, $u_\tau(t^+)/u_{\tau_b}$, starting from the time when the spanwise buffer layer blowing was terminated. This indicated that with respect to the wall shear stress, the boundary layer reaches its baseline state after $t^+ \approx 4000$ from the termination of the spanwise blowing. This evolution time reference will be noted with respect to other boundary layer characteristics in subsequent figures.

As had been shown in figure 8, the spanwise buffer layer blowing that resulted in the reduction of the wall shear stress produces an upward shift of the mean velocity profiles when scaled by inner variables. With this in mind, following the termination of the buffer

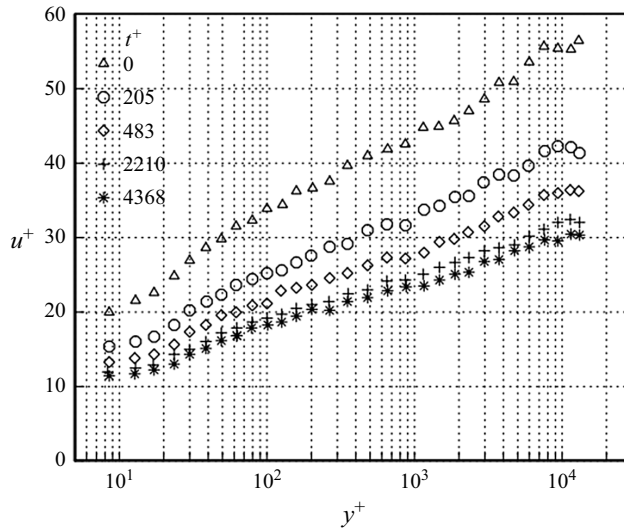


Figure 30. Temporal evolution of the mean velocity profiles scaled by inner variables following the termination of the spanwise buffer layer blowing.

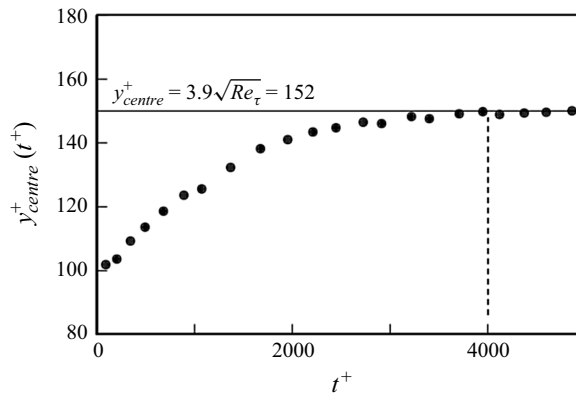


Figure 31. Temporal evolution of the mean velocity log profile centre following the termination of the spanwise buffer layer blowing.

layer blowing, [figure 30](#) shows the evolution of the mean velocity profiles back towards the zero-pressure-gradient canonical behaviour.

The temporal development of the geometric centre of the logarithmic region of the mean velocity profile in inner variables following the termination of the spanwise buffer layer blowing is shown in [figure 31](#). The significance of the geometric centre was highlighted by Mathis *et al.* (2009). Upon recovery to the baseline condition, the y^+ geometric centre asymptotes to a value of $3.9\sqrt{Re_\tau} = 152$. This appears to coincide with the asymptotic time scale of $t^+ = 4000$, which is noted on the plot.

The temporal evolution of the root mean square (r.m.s.) fluctuation levels of the three velocity components following the termination of the spanwise buffer layer blowing is shown in [figure 32\(a\)](#). These were measured at $y^+ = 15$ (Reynolds stress peak wall-normal location) that corresponded to $t^+ = 0$ in the boundary layer. The physical distance from the wall was adjusted to maintain a constant y^+ as $u_\tau(t^+)$ increased during the recovery

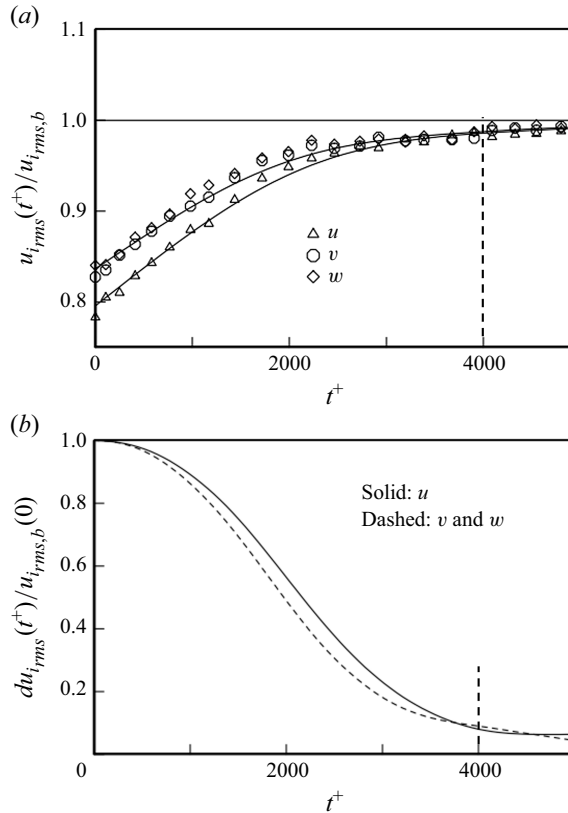


Figure 32. Temporal evolution of the ratios of the boundary layer velocity component fluctuation levels (a) and their rate of change (b) measured at $y^+ = 15$ that followed the termination of the spanwise buffer layer blowing.

to the baseline condition. The time rate of change of the r.m.s. fluctuation levels are shown in figure 32(b).

The three components of the velocity fluctuation appear to reach 98 % of the baseline level at $t^+ \approx 4000$, which indicates that their development slightly lags behind that of the mean flow. With regard to the redevelopment of the respective component fluctuation levels, based on the time rate of change, the v and w fluctuations both lag behind the u fluctuations. This is consistent with the fact that the turbulence production in the boundary layer transfers energy directly to the streamwise component, with the v and w components depending on pressure-strain rate terms to transfer energy to them from the streamwise component. The three components reach equal fluctuation levels at $t^+ \approx 4000$, but continue to exhibit growth beyond the $t^+ \approx 4000$. This is consistent with the fact that the characteristic turbulence time scales exceed that associated with the mean strain rate, which returned to the baseline sooner.

As previously discussed, the objective of the spanwise buffer layer blowing was to disrupt the autonomous near-wall cycle involving liftup and breakup of coherent streamwise vorticity associated with the low-speed wall streak structure and near-wall turbulence production. A metric of merit to the approach was a reduction in the wall-normal vorticity, ω_y , which was related to the spanwise mean flow distortion that flanked the elongated near-wall structures, and was subsequently deemed a critical parameter in the autonomous cycle involving streak transient growth (Schoppa & Hussain 2002).

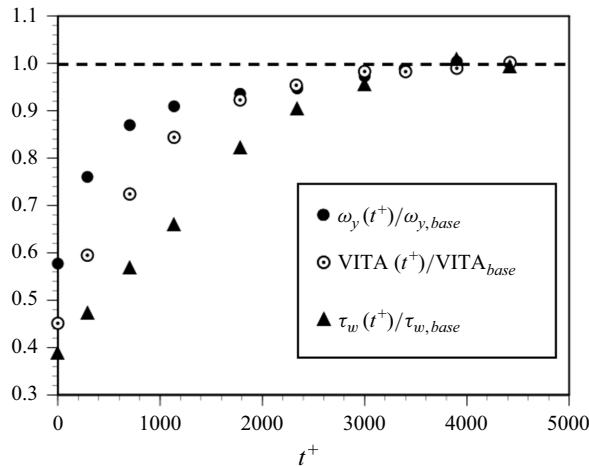


Figure 33. Temporal evolution of the ratios of the wall-normal vorticity component, number of VITA events and wall shear stress following the termination of the spanwise buffer layer blowing.

Considering the importance of this parameter to our objectives, [figure 33](#) documents the temporal growth of the wall-normal vorticity, ω_y , following the termination of the spanwise buffer layer blowing. The values shown are a spatial average within a 3-D region of $0 \leq y^+ \leq 20$ by $-250 \leq x^+ \leq 250$ by $0 \leq z^+ \leq 400$. This corresponds to the wall-normal vortical structures in the $[x^+, y^+ = 15, z^+]$ region that were visualized in [figure 24](#).

The detection of VITA events was used to perform the 3-D spatial ensemble-averaged velocity field reconstructions used in the calculation of vorticity components for the baseline and spanwise buffer layer blowing boundary layers. Therefore, it was also of interest to document the temporal evolution of the number of VITA events that occurred following the termination of the spanwise buffer layer blowing. [Figure 33](#) shows the temporal evolution of the number of VITA events along with the temporal evolution of the wall-normal vorticity component, ω_y , and the wall shear stress, τ_w . [Figure 33](#) highlights the significant link between the level of wall-normal vorticity, the frequency of turbulence producing VITA events, and subsequently the wall shear stress. Although all of these exhibit a similar growth with t^+ following the termination of the spanwise buffer layer blowing, it is important to note that the temporal recovery of ω_y leads that of the number of VITA events and the increase in the wall shear stress. This observation is consistent with the autonomous near-wall mechanism shown schematically in [figure 1](#) whereby increased levels of wall-normal vorticity are required to increase the production of streamwise vorticity which, in turn, gives rise to an increase in the number of VITA ejection-sweep events that has been shown to be tied to the level of the wall shear stress (Kline *et al.* 1967).

Viewed from the standpoint of an instability mechanism of the distorted mean flow, of which ω_y is a critical parameter, one might expect a sharp delineation between stable and unstable regimes which is not apparent in [figure 33](#). However, it must be remembered that the conditional measurements were based upon VITA event detections in both the baseline and actuated flows. Hence, it is to be expected that even in the actuated flow, the level of ω_y was within the unstable regime for streak transient growth in the sense that longitudinal streamwise buffer layer vorticity still existed in the actuated flow and produced VITA events, but at a lower frequency and level.

Another metric of practical interest is the convective distance over which the boundary layer characteristics recover from the termination of the spanwise buffer layer blowing. In channel flow DNS simulations, Schoppa & Hussain (1998) had shown that the region of sustained drag reduction would extend to $x^+ \simeq 16\,000$. In direct drag measurements using oil film interferometry, Thomas *et al.* (2019) found good agreement with that prediction. However, the level of drag reduction in that early experiment used less optimized actuator conditions, producing only a 6 % reduction in u_τ .

As indicated, aside from the turbulence fluctuations, the recovery to the baseline boundary layer characteristics following the termination of the spanwise buffer layer blowing nominally occurred in $t^+ \approx 4000$. The values of t^+ were based upon the recorded time varying values of u_τ , which corresponded to a physical time of 2.5 s, or a corresponding $T^* = tU_\infty/\delta = 82$. Assuming a convective speed of $U_c \approx 0.7U_\infty$, the corresponding streamwise fetch associated with the return to the baseline state was $x \approx 66\delta$. This result is encouraging in terms of practical implementation for large-scale drag reduction. The inner-variable scaled streamwise recovery distance base on $t^+ = 4000$ is $x^+ = U_c^+ t^+ \approx 86\,000$, which is considerably larger than that reported by Schoppa & Hussain (1998). This is not surprising since it is likely to be associated with the significantly higher reduction in the friction drag and turbulent stresses obtained in the present study which would naturally lead to a larger recovery distance.

4. Conclusions

The results of two experiments are reported. Both were motivated by the intent to reduce TBL friction drag by intervening in the near-wall streak transient growth mechanism. The first focused on the effect of spanwise buffer layer blowing on the time-averaged (mean) characteristics of TBLs over a range of free stream velocities of $17 - 51 \text{ m s}^{-1}$ and momentum thickness Reynolds numbers from 6000 to 12 500. These measurements were primarily designed to relate the changes in the mean boundary layer characteristics to the buffer layer blowing design elements.

The buffer layer blowing was performed using a flush surface array of pulsed-DC plasma actuators. The pulsing frequency was 500 Hz and the pulse width during which the actuator draws power, was $O\,10^{-7}$ s. The maximum power supplied to the actuator array was 7.47 W which when distributed over the 0.524 m^2 array area gave a power density 0.014 W m^{-2} . The 500 Hz pulsing frequency was not related to any cycle characteristic time scales of the baseline boundary layer, and experiments in still air indicated that it induced a steady spanwise directed wall jet. For the range of boundary layer conditions examined, the majority of the plasma actuator induced velocity was intentionally confined within the buffer layer, and the peak velocity was of the order of the baseline friction velocity, u_τ .

Although performed in two different wind tunnels, both experiments utilized the same wall shear force measuring system. This consisted of a 22.86 cm square floating platen that was flush mounted in the test section floor, at the centre span of the two identical test sections. The platen was mounted on linear air bearings that only allowed motion in the streamwise direction and therefore measured the streamwise component of the wall shear stress. The shear force on the platen was measured with interchangeable cantilever style load cells with full-scale ranges that were optimized for the different free stream conditions. The area under the platen assembly including the air bearings and load cells was fully enclosed and sealed to prevent any air leaks from affecting the shear stress measurement. In addition, any effects of electronic noise or electrostatic forces were identified and fully eliminated.

The spanwise buffer layer blowing resulted in a significant reduction of the wall shear stress that was reflected in a lowering of the wall shear velocity, u_τ . This produced an upward shift of the mean velocity profiles when scaled by inner variables. Additionally, the slope of the log layer was also affected by the spanwise buffer layer blowing. This effectively changed the von Kármán coefficient and additive constant. This result was fully consistent with the reduction in the mean strain rate at the wall that gave rise to a reduction in the wall shear stress. This, in turn, was a consequence of reduced wall-directed fluid transport associated with a weakening of buffer layer streamwise vorticity.

Although the degree to which u_τ was lowered was a function of the pulsed-DC voltage, which determined the maximum spanwise blowing velocity, \overline{W}_{max} , the greater dependence was on the inner variable spacing between electrodes (blowing sites) in the actuator array. This was demonstrated for the range $1000 \leq \lambda_z^+ \leq 3000$ for which $0.48 \leq u_{\tau_{plasma}}/u_{\tau_{baseline}} \leq 0.90$, respectively. The reduction in u_τ varied logarithmically with λ_z^+ which is consistent with the relative change in friction velocity being inversely proportional to the number of low-speed streaks being simultaneously controlled between adjacent electrodes.

The second experiment was designed to document the effect of the spanwise buffer layer blowing on the unsteady TBL characteristics and coherent structures. This was performed in a boundary layer that was developed to provide sufficiently high spatial resolution for the dual sensor hot-wire probes used in the experiment. The pulsed-DC actuator array used in these experiments was the same as in the other experiment with the exception of having a smaller electrode spacing with a $\lambda_z^+ \approx 300$. The pulsing frequency and pulse width were the same as in the previous experiment, but the DC voltage was set to where the largest reduction in u_τ occurred. In that case, $u_{\tau_{plasma}}/u_{\tau_{baseline}} = 0.38$ which corresponded to a 62 % reduction in the viscous drag.

Velocity measurements involved $[u, v]$ and $[u, w]$ hot-wire sensors that surveyed $[y, z]$ space with time converted to a pseudospacial coordinate, $[x]$. These documented reductions throughout the boundary layer thickness of all components of the Reynolds stress. When spatially averaged across the boundary layer, the largest effect of the buffer layer blowing was on the v -component fluctuations which decreased by 21 %, followed by the u -component fluctuations that decreased by 18 % and the w -component fluctuations that decreased by 13 %. Local peak value reductions in the near-wall region were higher with the largest for the streamwise component, u , as was shown in [figure 18](#).

Conditional-averaged reconstructions of the 3-D flow field were performed to assess the effect that the spanwise sublayer blowing had on the streamwise vorticity, ω_x , that is associated with the near-wall ‘streak’ structure (Kline *et al.* 1967), and the wall-normal vorticity, ω_y , which is considered a critical parameter in the ‘streak transient growth’ mechanism (Schoppa & Hussain 2002). Both of the vorticity components were significantly reduced by the buffer layer blowing. In particular, when averaged over a 3-D region within $-250 \leq x^+ \leq 250$ by $0 \leq y^+ \leq 20$ by $0 \leq z^+ \leq 400$, ω_y was reduced by 58 %. The reduction in ω_y was associated with a significant reduction of the streamwise vorticity which as shown in [figure 26](#) is especially evident in the sublayer.

The temporal response of the boundary layer following the termination of the buffer layer blowing was documented with the goal of providing some insight into the time scales related to mechanisms of turbulence production. The time-varying wall shear stress, $\tau_w(t^+)$ was obtained from the drag measuring platen and used to calculate the time-dependent shear velocity, $u_\tau(t^+)$. After terminating the buffer layer blowing, it reached the baseline boundary layer state at $t^+ \approx 4000$. The mean velocity profiles, frequency of VITA detected ‘ejection-sweep’ events, and ω_y vorticity similarly recovered with the same time scale. With regard to the turbulent velocity fluctuations, at $t^+ = 4000$, the three

components reached 98 % of their baseline levels, which indicated that their development slightly lagged behind that of the mean flow. The recovery of the v and w fluctuating velocity lagged that of the u component velocity until $t^+ \approx 3000$. This is consistent with the fact that production of turbulence in the boundary layer channels energy first into the streamwise fluctuation which is then redistributed to the other components via pressure-strain rate terms.

Recent experiments by Cheng *et al.* (2021) and Wei & Zhou (2024) that utilized a wall-mounted array of dielectric-barrier-discharge plasma actuators to generate near-wall spanwise blowing have provided a valuable data set to which to compare our results. Their actuator arrangement followed our designs with the exception that rather than unidirectional blowing they utilized a spanwise-opposed wall jet configuration that we have also previously utilized (Duong 2019; Thomas *et al.* 2019; Thomas *et al.* 2023) and have shown to also be effective in lowering the viscous drag. Another incidental difference is that they operated the plasma actuators with an AC waveform rather than in our case, a pulsed-DC waveform, with the latter being far more energy efficient.

As in our experiments, Cheng *et al.* (2021) and Wei & Zhou (2024) performed direct drag measurements using a floating-element force balance. Of particular note with regard to scaling was that their range of Re_τ was an approximately an order-of-magnitude lower than in our experiments, and their spanwise blowing velocities were up to five times larger than in our experiments.

Cheng *et al.* (2021) and Wei & Zhou (2024) corroborated all of our observations including a plasma actuator optimum voltage (controlling the spanwise blowing velocity) that was a function of Re_τ , at which they reported up to a 75 % reduction in the viscous drag; an increase in the von Kármán coefficient, a reduction in the u , v -Reynolds stress and turbulence energy production that accompanied the drag reduction; and a reduction in the ‘ejection’ portion of the VITA signature that accompanied the spanwise blowing, all of which Cheng *et al.* (2021) found to be ‘consistent with the stabilized streaks’.

The large difference in the range of Re_τ between those (Cheng *et al.* 2021; Wei & Zhou 2024) and the present experiments provided an opportunity to further investigate the actuator scaling relations for the spanwise buffer layer blowing effect. This initially involved data from Wei & Zhou (2024) that documented the change in the viscous drag as a function of Re_τ for their highest plasma actuator voltage, $E_{p-p} = 5.6$ and 6 kV. For a fixed physical spacing of the surface electrodes, the different Re_τ values resulted in different effective electrode spacing when normalized by inner variables, λ_z^+ . For consistency in the comparison, and to account for their use of opposed wall jets, the appropriate physical spacing was taken to be the distance between each exposed electrode and the centre of the interelectrode gap. As was shown in figure 13, their data and the present data, representing the level of viscous drag reduction for two disparate ranges of shear-stress Reynolds numbers, collapse remarkably well when the inner variable electrode spacing, λ_z^+ , was normalized by their respective baseline Re_τ values. This was equivalent to normalizing the physical electrode spacing, λ_z , by the TBL thickness, δ .

As shown in figure 14, differences in the actuator blowing velocities on the viscous drag reduction between the those of Wei & Zhou (2024), and in the present results (indicated by the ND data) were found to disappear when the actuator blowing velocity in inner variables, W_{max}^+ , was scaled by the corresponding Re_τ . This scaling was equivalent to the physical spanwise blowing velocity Reynolds number, $W_{max}\delta/\nu$.

Comparisons like these were not only beneficial in further validating the results, but are also extremely important in the gained understanding of the flow physics underlying TBLs. Additionally, the two types of plasma actuators used in these studies offer a simple methodology to produce the spanwise buffer layer blowing. Knowing the scaling with

Reynolds number and blowing velocity, opens the opportunity for other approaches such as the use of compressed air tangential jets investigated by Zhang *et al.* (2024).

Finally, the temporal response of the boundary layer following the termination of the buffer layer blowing was documented with the hope of providing insight into the relative time scales related to mechanisms for turbulence production. The time-varying wall shear stress, $\tau_w(t^+)$ was obtained from the drag measuring platen and used to calculate the temporal variation of the shear velocity, $u_\tau(t^+)$. After terminating the buffer layer blowing, it reached the baseline boundary layer state in $t^+ \approx 4000$.

As was shown in figure 33, the temporal growth of wall-normal vorticity, the number of VITA events and the wall shear stress all reached asymptotic final states by $t^+ \approx 4000$. Of particular interest was the observation that the wall-normal vorticity growth led that of the VITA events which, in turn, led the wall shear stress growth. This observation is consistent with the autonomous near-wall mechanism that was shown in figure 1 in which streak transient growth shows that ω_y leads to the rapid growth of near-wall streamwise vortices whose instability gives rise to VITA burst-sweep events which in turn, gives rise to higher levels of viscous drag. The turbulent stresses were within 98 % of their final baseline values by $t^+ \approx 4000$. In this case the growth of the streamwise normal stress led that of the v and w -components.

A metric of interest discussed in § 1 was the convective distance over which the boundary layer characteristics recovered from the termination of the buffer layer blowing. In DNS channel flow simulations, Schoppa & Hussain (1998) had shown that the region of sustained drag reduction would extend to $x^+ \simeq 16\,000$. In direct drag measurements using oil film interferometry, Thomas *et al.* (2019) found good agreement with that prediction. However, in that early experiment the actuator condition was less optimized, producing only a 6 % reduction in u_τ . The question was if the extent of sustained drag reduction depended on its initial level. In work reported here, the drag reduction was an order of magnitude larger.

Aside from the turbulence fluctuations, the recovery to the baseline boundary layer characteristics following the termination of the spanwise buffer layer blowing occurred in $t^+ \approx 4000$. The values of t^+ were based upon the recorded, time varying values of u_τ . Assuming a convective speed of $U_c \approx 0.7U_\infty$, the corresponding streamwise fetch associated with return to the baseline state was $x \approx 66\delta$. This result is encouraging in terms of practical implementation for large-scale drag reduction.

Declaration of interest. The authors report no conflict of interest.

REFERENCES

- BAARS, W., SQUIRE, D., TALLURU, K., ABBASSI, M., HUTCHINS, N. & MARUSIC, I. 2016 Wall-drag measurements of smooth-and rough-wall turbulent boundary layers using a floating element. *Exp. Fluids* **57** (5), 90.
- BARON, A. & QUADRIO, M. 1996 Turbulent drag reduction by spanwise wall oscillations. *Appl. Sci. Res.* **55** (4), 311–326.
- BLACK, T. 1966 The structure of wall turbulence. In *Proceedings of the Heat Transfer and Fluid Mechanics Institute* (ed M. Saad & J. Miller), pp. 366. Stanford University Press.
- BLACKWELDER, R. & ECKELMAN, H. 1979 Streamwise vortices associated with the bursting phenomenon. *J. Fluid Mech.* **94** (3), 577–594.
- BLACKWELDER, R. & KAPLAN, R. 1976 On the wall structure of the turbulent boundary layer. *J. Fluid Mech.* **76** (1), 89–112.
- BLACKWELDER, R. & WOO, H. 1974 Pressure perturbation of a turbulent boundary layer. *Phys. Fluids* **17** (3), 515–519.
- CANTON, J., ÖRLÜ, R., CHIN, C., SCHLATTER, P. 2016 Reynolds number dependence of large-scale friction control in turbulent channel flow. *Phys. Rev. Fluids* **1** (8), 081501.

- CHENG, X., WONG, C., HUSSAIN, F., SCHRODER, W. & ZHOU, Y. 2021 Flat plate drag reduction using plasma-generated streamwise vortices. *J. Fluid Mech.* **918** (A24), 1–37.
- CHOI, J., CHUN-XIAO, X. & SUNG, H. 2002 Drag reduction by spanwise wall oscillation in wall-bounded turbulent flows. *AIAA J.* **40** (5), 842–850.
- CHOI, K.-S. & CLAYTON, B.R. 2001 The mechanism of turbulent drag reduction with wall oscillation. *Intl J. Heat Fluid Flow* **22** (1), 1–9.
- CORINO, E.R. & BRODKEY, R.S. 1969 A visual investigation of the wall region in turbulent flow. *J. Fluid Mech.* **1** (1), 1–30.
- CORKE, T., NAGIB, H. & GUEZENNEC, Y. 1981 Modification in drag of turbulent boundary layers resulting from manipulation of large-scale structures. Technical Report NASA Contractor Report 3444. NASA.
- CORKE, T.C., ENLOE, C.L. & WILKINSON, S.P. 2010 Dielectric barrier discharge plasma actuators for flow control. *Annu. Rev. Fluid Mech.* **42** (1), 505–529.
- DHANAK, M. & SI, C. 1999 On reduction of turbulent wall friction through spanwise oscillations. *J. Fluid Mech.* **383**, 175–195.
- DOLIGALSKI, T., SMITH, C. & WALKER, J. 1980 Production mechanism for turbulent boundary layer flows, viscous drag reduction. *Prog. Aeronaut. Astronaut.* **72**, 47–72.
- DUONG, A. 2019 Active turbulent boundary layer control: An experimental evaluation of viscous drag reduction using pulsed-dc plasma actuators. *Ph.D Thesis*, University of Notre Dame, USA.
- DUONG, A., CORKE, T., THOMAS, F. & DISSER, K. 2018 Active turbulent boundary layer drag reduction using pulsed-dc plasma actuator. In *AIAA Scitech Forum, AIAA Paper 2018-1357*.
- DUONG, A., CORKE, T. & THOMAS, F. 2021 Characteristics of drag-reduced turbulent boundary layers with pulsed-direct-current plasma actuation. *J. Fluid Mech.* **915** (A113), 1–29.
- EINSTEIN, H. & LI, H. 1956 The viscous sublayer along a smooth boundary. *Trans. Am. Soc. Civil Eng.* **123**, 293–313.
- HAMILTON, J., KIM, J. & WALEFFE, F. 1995 Regeneration mechanisms of turbulence near wall structure. *J. Fluid Mech.* **287**, 317–489.
- HANRATTY, T. 1956 Turbulent exchange of mass and momentum with a boundary. *J. Am. Inst. Chem. Engrs* **2** (3), 359–362f.
- HUANG, J., CORKE, T. & THOMAS, F. 2006a Plasma actuators for separation control of low-pressure turbine blades. *AIAA J.* **44** (1), 51–57.
- HUANG, J., CORKE, T. & THOMAS, F. 2006b Plasma actuators for separation control of low-pressure turbine blades. *AIAA J.* **44** (7), 1477–1487.
- HUTCHINS, N. & MARUSIC, I. 2007a Evidence of very long meandering features in the logarithmic region of turbulent boundary layers. *J. Fluid Mech.* **579**, 1–28.
- HUTCHINS, N. & MARUSIC, I. 2007b Large-scale influences in near-wall turbulence. *Phil. Trans. R. Soc. A: Math. Phys. Engng Sci.* **365** (1852), 647–664.
- JASINSKI, C. & CORKE, T.C. 2020 Mechanism for increased viscous drag over porous sheet acoustic liners. *AIAA J.* **58** (8), 3393–3404.
- JIMENEZ, J. & MOIN, P. 1991 The minimal flow unit in near wall turbulence. *J. Fluid Mech.* **225**, 213–240.
- JIMENEZ, J. & PINELLI, A. 1999 The autonomous cycle of near-wall turbulence. *J. Fluid Mech.* **389**, 335–359.
- KIM, J. 2011 Physics and control of wall turbulence for drag reduction. *Phil. Trans. R. Soc. A: Math. Phys. Engng Sci.* **369** (1940), 1396–1411.
- KLEBANOFF, P.S. 1954 Characteristics of turbulence in a boundary layer with zero pressure gradient. NACA Technical Note No. 3178.
- KLINE, S., REYNOLDS, W., SCHRAUB, F. & RUNSTADLER, P. 1967 The structure of turbulent boundary layers. *J. Fluid Mech.* **30** (4), 741–773.
- MATHIS, R., HUTCHINS, N. & MARUSIC, I. 2009 Large-scale amplitude modulation of small-scale structures in turbulent boundary layers. *J. Fluid Mech.* **628**, 311–337.
- MATHIS, R., HUTCHINS, N. & MARUSIC, I. 2011 A predictive inner-outer model for streamwise turbulence statistics in wall-bounded flows. *J. Fluid Mech.* **681**, 537–566.
- MATLIS, E. H. 2003 Controlled experiments on instabilities and transition to turbulence on a sharp cone at Mach 3.5. Ph.D. Thesis, University of Notre Dame, Notre Dame, IN.
- MEYERS, A. 2023 Active boundary layer control: an experimental investigation in turbulent boundary layer skin-friction drag reduction using pulsed dc plasma actuator. Ph.D. Thesis, University of Notre Dame, Notre Dame, IN.
- QUADRIO, M. & SIBILLA, S. 2011 Numerical simulation of flow in a pipe oscillating around its axis. *J. Fluid Mech.* **424**, 217–241.
- RAO, K., NARASHIMA, R. & NARAYANAN, M. 1971 The bursting phenomenon in a turbulent boundary layer. *J. Fluid Mech.* **48** (2), 339–352.

- RICCO, P., SKOTE, M. & LESCHZINER, M. 2021 A review of turbulent skin-friction drag reduction by near-wall transverse forcing. *Prog. Aerosp. Sci.* **123**, 100713.
- ROBINSON, S. 1991 Coherent motions in the turbulent boundary layer. *Annu. Rev. Fluid Mech.* **23** (1), 601–639.
- SAVILL, A. & MUMFORD, J. 1988 Manipulation of turbulent boundary layers by outer-layer devices: skin friction and flow-visualization result. *J. Fluid Mech.* **191**, 389–418.
- SCHOPPA, W. & HUSSAIN, F. 1998 A large-scale control strategy for drag reduction in turbulent boundary layers. *Phys. Fluids* **10** (5), 1049–1051.
- SCHOPPA, W. & HUSSAIN, F. 2002 Coherent structure generation in near-wall turbulence. *J. Fluid Mech.* **453**, 57, 108–108.
- TAN-ATICHAT, J. & NAGIB, H. 1976 Wind tunnel simulation of neutral atmospheric surface layers by the counter-jet technique. *J. Air Pollut. Control Assoc.* **26** (7), 668–673.
- THOMAS, F., CORKE, T. & DUONG, A. 2023 Airfoil friction drag reduction with net power savings using pulsed-direct-current plasma actuation. *AIAA J.* **61** (9), 4045–4055.
- THOMAS, F.O., CORKE, T.C., DUONG, A., MIDYA, S. & YATES, K. 2019 Turbulent drag reduction using pulsed-dc plasma actuation. *J. Phys. D: Appl. Phys.* **52** (43), 434001.
- TRUJILLO, S., BOGARD, D. & BALL, K. 1997 Turbulent boundary layer drag reduction using an oscillating wall. In *28th AIAA Fluid Dynamics Conference, 4th AIAA Shear Flow Control Conference, Snowmass, CO*. Paper 1997-187.
- WEI, X. & ZHOU, Y. 2024 Scaling of drag reduction in a turbulent boundary layer based on plasma-generated streamwise vortices. In *13th International Symposium on Turbulence Shear Flow Phenomena (TSFP13)*, Montreal, Canada, June 25–28.
- YAO, J., CHEN, X., THOMAS, F. & HUSSAIN, F. 2017 Large-scale control for drag reduction in turbulent channel flows. *Phys. Rev. Fluids* **2** (6), 062601.
- ZHANG, X., WEI, X., ZHANG, E., WANG, H. & ZHOU, Y. 2024 Wall-normal-microjet-based drag reduction of high Reynolds number turbulent boundary layers. In *13th International Symposium on Turbulence Shear Flow Phenomena (TSFP13)*, Montreal, Canada, June 25–28.